Atmospheric Research 228 (2019) 223–241

Contents lists available at ScienceDirect

Atmospheric Research

journal homepage: www.elsevier.com/locate/atmosres

Extreme, wintertime Saharan dust intrusion in the Iberian Peninsula: Lidar monitoring and evaluation of dust forecast models during the February 2017 event

Alfonso J. Fernández[a], Michäel Sicard[b,c,*], Maria J. Costa[d], Juan L. Guerrero-Rascado[e,f], José L. Gómez-Amo[g], Francisco Molero[a], Rubén Barragán[b,c], Sara Basart[h], Daniele Bortoli[d], Andrés E. Bedoya-Velásquez[e,f], María P. Utrillas[g], Pedro Salvador[a], María J. Granados-Muñoz[b,1], Miguel Potes[d], Pablo Ortiz-Amezcua[e,f], José A. Martínez-Lozano[g], Begoña Artíñano[a], Constantino Muñoz-Porcar[b], Rui Salgado[d], Roberto Román[e,f,i], Francesc Rocadenbosch[b,c], Vanda Salgueiro[d], José A. Benavent-Oltra[e,f], Alejandro Rodríguez-Gómez[b], Lucas Alados-Arboledas[e,f], Adolfo Comerón[b], Manuel Pujadas[a]

[a] Department of Environment, Research Centre for Energy, Environment and Technology (CIEMAT), Madrid, Spain
[b] Department of Signal Theory and Communications, CommSensLab, Universitat Politècnica de Catalunya, Barcelona, Spain
[c] Ciències i Tecnologies de l'Espai - Centre de Recerca de l'Aeronàutica i de l'Espai/Institut d'Estudis Espacials de Catalunya (CTE-CRAE/IEEC), Universitat Politècnica de Catalunya, Barcelona, Spain
[d] Institute of Earth Sciences and Department of Physics, ECT and IIFA, Universidade de Évora, Évora, Portugal
[e] Department of Applied Physics, University of Granada, Granada, Spain
[f] Andalusian Institute for Earth System Research (IISTA-CEAMA), Granada, Spain
[g] Department of Physics of the Earth and Thermodynamics, University of Valencia, Valencia, Spain
[h] Earth Sciences Department, Barcelona Supercomputing Center (BSC), Barcelona, Spain
[i] Atmospheric Optic Group (GOA), University of Valladolid, Valladolid, USA

ARTICLE INFO

Keywords:
Extreme Saharan dust intrusion
Particle optical properties
Sun-photometer
Multi-wavelength lidar
Dust forecast model
Model evaluation
Vertical distribution

ABSTRACT

An unprecedented extreme Saharan dust event was registered in winter time from 20 to 23 February 2017 over the Iberian Peninsula (IP). We report on aerosol optical properties observed under this extreme dust intrusion through passive and active remote sensing techniques. For that, AERONET (AErosol RObotic NETwork) and EARLINET (European Aerosol Research LIdar NETwork) databases are used. The sites considered are: Barcelona (41.38°N, 2.17°E), Burjassot (39.51°N, 0.42°W), Cabo da Roca (38.78°N, 9.50°W), Évora (38.57°N, 7.91°W), Granada (37.16°N, 3.61°W) and Madrid (40.45°N, 3.72°W). Large aerosol optical depths (AOD) and low Ångström exponents (AE) are observed. An AOD of 2.0 at 675 nm is reached in several stations. A maximum peak of 2.5 is registered in Évora. During and around the peak of AOD, AEs close to 0 and even slightly negative are measured. With regard to vertically-resolved aerosol optical properties, particle backscatter coefficients as high as 15 $Mm^{-1} sr^{-1}$ at 355 nm are recorded at the lidar stations. Layer-mean lidar ratios are found in the range 40–55 sr at 355 nm and 34–61 sr at 532 nm during the event. The particle depolarization ratios are found to be constant inside the dust layer, and consistent from one site to another. Layer-mean values vary in the range 0.19–0.31. Another remarkable aspect of the event is the limited vertical distribution of the dust plume which never exceeds 5 km. The extreme aspect of the event also presented a nice case for testing the ability of two dust forecast models, BSC-DREAM8b and NMMB/BSC-Dust, to reproduce the arrival, the vertical distribution and the intensity of the dust plume over a long-range transport region. In the particular case of the February 2017 dust event, we found a large underestimation in the forecast of the extinction coefficient provided by BSC-DREAM8b at all heights independently of the site. In contrast NMMB/BSC-Dust forecasts presented a better agreement with the observations, especially in southwestern part of the IP. With regard to the forecast skill as a function of lead time, no clear degradation of the prognostic is appreciated at 24, 48 and 72 h for Évora and Granada stations (South). However the prognostic does degrade (bias increases and/or correlation decreases) for Barcelona

* Corresponding author at: Department of Signal Theory and Communications, CommSensLab, Universitat Politècnica de Catalunya, Barcelona, Spain.
E-mail address: msicard@tsc.upc.edu (M. Sicard).
[1] Now at: Andalusian Institute for Earth System Research (IISTA-CEAMA), Granada, Spain

https://doi.org/10.1016/j.atmosres.2019.06.007
Received 13 March 2019; Received in revised form 7 June 2019
Available online 18 June 2019

(North), which is attributed to the fact that Barcelona is at a greater distance from the source region and to the singularity of the event.

1. Introduction

Mineral aerosols are usually originated over arid or semiarid regions as a consequence of continuous soil erosion produced by wind. The strong warming of desert areas during daytime produces vertical thermal turbulences that can reach altitudes of up to 5 km, followed by periods of nocturnal stability (Santos et al., 2013). Massive resuspension of huge amounts of mineral aerosols are thus produced and can be transported long distances by different mechanisms. Forty percent of the aerosol mass emitted into the troposphere is attributed to desert dust and it is considered as the second largest source of natural aerosols, after sea salt (Andreae, 1995; IPCC, 2001; Salvador et al., 2014). The main desert dust sources is the Sahara desert since it is responsible for more than half of the world atmospheric mineral dust (Prospero et al., 2002; Mahowald et al., 2005; Wagner et al., 2009; Salvador et al., 2016). Under specific synoptic meteorological situations, a large amount of Saharan dust is transported towards the Mediterranean basin over which the planetary boundary layer is usually relatively shallow (Lafontaine et al., 1990; Obregón et al., 2015; Khan et al., 2015; Cuevas et al., 2017).

In the last two decades the number of surveys addressing the study of atmospheric mineral aerosols, especially around the Mediterranean basin, has increased for several reasons. Firstly, from the climate change standpoint, mineral aerosols play an important role on the atmospheric radiative budget through scattering and absorption of the incoming solar and outgoing infrared radiation, and they act as cloud condensation nuclei (Klein et al., 2010; IPCC, 2013). Their large temporal and spatial variability is responsible for a high uncertainty degree in aerosol radiative forcing estimates (Forster et al., 2007; Boucher et al., 2013). Secondly, from the point of view of air quality, it has been demonstrated that African dust is the main particle source, contributing to the regional background levels of PM_{10} across the Mediterranean (35–50% of PM_{10}) with maximum contributions up to 80% of the total PM_{10} mass (Pey et al., 2013). The sporadic but intense natural contributions of PM have been responsible for a high number of exceedances of the PM_{10} daily limit value (50 $\mu g/m^3$, according to the 2008/50/EC European Directive) as registered in different rural and urban monitoring sites across the Mediterranean Basin (Querol et al., 2009; Salvador et al., 2013).

The large temporal and spatial variability of mineral dust in the atmosphere mentioned earlier makes its systematic monitoring a difficult task which, as of today, still represents a problematic issue that the scientific community, and especially the observation and modelling communities, are trying to address. Some works based on long-term databases have indicated that the Mediterranean basin is affected by African dust intrusions following a marked seasonal pattern (Mona et al., 2006; Salvador et al., 2013; Pey et al., 2013; Sicard et al., 2016): summer prevalence has been detected in the western part; no seasonal trend has been observed in the central region and higher contributions of desert dust have been commonly produced in spring-early summer in the eastern part of the basin. Very recently an increasing number of works have reported statistics and tendency of intense (i.e. strong and extreme) Saharan dust events in the Mediterranean Basin. At a given site and for a given aerosol optical depth (AOD) climatology (from either ground- or satellite-based sensors), Gkikas et al. (2013) suggested to define strong and extreme events with two threshold levels defined as a function of the mean (Mean) and standard deviation (Std) of the AOD: Mean + 2 x Std and Mean + 4 x Std. Strong events fulfil Mean + 2 x Std ≤ AOD < Mean + 4 x Std, and extreme events fulfil AOD ≥ Mean + 4 x Std. To get an idea of the low probability of occurrence of strong and extreme mineral dust events in winter, Gkikas et al. (2013) calculated the seasonal frequency of occurrence in the western Mediterranean Basin over land and for the period 2000–2007 of strong and extreme events to be 1 and 1.2%, respectively. In spite of this small percentage, two relevant strong and extreme mineral dust events (following the definition of Gkikas et al. (2013)) have been recorded in the last three years in the Iberian Peninsula (IP) during the winter season. In February 2016 a strong event (AOD ~ 0.4) affecting the whole IP has been documented with in situ/remote sensing instrumentation (Titos et al., 2017), ceilometers (Cazorla et al., 2017) and in-situ/AERONET/satellite instrumentation (Sorribas et al., 2017). In February 2017 an exceptionally extreme event (AOD > 2.0) affected again the whole IP, as examined with AERONET and MPLNET (Micro Pulse Lidar Network) lidars by Córdoba-Jabonero et al. (2019). The mineralogy of the event has been reported by Rodríguez-Navarro et al. (2018). The prediction of extreme dust intrusions by dust forecast models has only been treated seldomly in the literature (Huneeus et al., 2016, event with an AOD ~ 1.0; Ansmann et al., 2017, AOD ~ 0.6; Tsekeri et al., 2017, AOD ~ 0.4) as compared to single moderate events or long-term database of events independently of their intensity (Gobbi et al., 2013; Santos et al., 2013; Mona et al., 2014; Binietoglou et al., 2015; Sicard et al., 2015). However such predictions are essential to warn populations in advance and set plans to mitigate the severe effects that high levels of particulate matter may cause to lives and property.

In this article, we report on the extreme dust event that hit the Iberian Peninsula (IP) on 20–23 February 2017. The aim of the paper is twofold: 1) to provide an overview of the 4D spatio-temporal evolution of the dust optical properties observed by remote sensing instruments throughout the IP, and 2) to evaluate the capabilities of dust transport models to reproduce such extreme dust events. The paper is organized as follows: the instruments and methodology are briefly described in Section 2. Section 3 deals with the description of the synoptic situation and columnar aerosol optical properties from sun and sky photometers. In Section 4, vertically-resolved optical properties are discussed. Section 5 presents the performance of the dust models. Finally, conclusions can be found in Section 6.

2. Instruments and methodology

2.1. AERONET sun-photometers in the IP

The AErosol RObotic NETwork (AERONET) is a global ground-based network of sun/sky multi-wavelength CIMEL CE-318 sun-photometers that provides long-term records of atmospheric columnar aerosol optical properties (Holben et al., 1998). The CIMEL spectral sun-photometer measures the direct solar irradiances with a field of view of approximately 1.2° and the sky radiances (in the almucantar and principal plane scenarios), at several spectral channels (see Table 1). The direct-sun measurements are used to obtain the spectral AOD, Ångström exponent at several wavelength pairs and precipitable water vapor, approximately every 15 min. The AOD uncertainty, mainly due to the calibration, is estimated to vary between 0.01 and 0.02 (Holben et al., 1998).

The sky radiance measurements can be inverted to estimate aerosol optical properties such as the size distribution, the percentage of spherical particles in the aerosol mixture, several microphysical parameters describing the total, fine and coarse aerosol modes and numerous spectral quantities: complex refractive index, single scattering albedo, phase function, asymmetry parameter, extinction and absorption optical depths. The aerosol properties retrieved are also used for calculating the broad-band fluxes at the bottom and top of the

Table 1
Summary of the sites considered in the study: main characteristics of the AERONET sun-photometers and EARLINET lidars used.

Site	Long.	Lat.	Altitude	AERONET		EARLINET				
				Wavelengths		Elastic wavelengths	Raman wavelengths	Vertical resolution	Start time	Stop time
	(°)	(°)	(m a.s.l.)	(nm)		(nm)	(nm)	(m)	(UTC)	(UTC)
BA	2.11 E	41.39 N	115	440, 675, 870, 1020		355, 532 total, 532 cross, 1064	387, 407, 607	3.75	08:11 (23 Feb)	23:54 (23 Feb)
BU	0.42 W	39.51 N	60	340, 380, 440, 500, 675, 870, 1020, 1640		355 cross and parallel	387	15	No measurements available	
CR	9.50 W	38.78 N	140	340, 380, 440, 500, 675, 870, 1020		No lidar available				
EV	7.91 W	38.57 N	293	340, 380, 440, 500, 675, 870, 1020		355, 532, 532 cross, 1064	387, 607	30	00:00 (20 Feb)	23:59 (23 Feb)
GR	3.61 W	37.16 N	680	340, 380, 440, 500, 675, 870, 1020		355, 532 parallel, 532 cross, 1064	387, 407, 607	7.5	12:00 (20 Feb)	18:00 (20 Feb)
									19:00 (20 Feb)	21:00 (20 Feb)
									07:31 (21 Feb)	14:21 (21 Feb)
									07:31 (22 Feb)	20:00 (22 Feb)
MA	3.72 W	40.45 N	669	340, 380, 440, 500, 675, 870, 1020		355, 532, 1064	387, 407, 607	7.5 (elastic) 3.75 (Raman)	21:00 (22 Feb)	23:36 (22 Feb)
									05:00 (23 Feb)	08:00 h UTC (23 Feb)
									11:00 (23 Feb)	11:52 (23 Feb)

The site acronyms are: BA for Barcelona, BU for Burjassot, CR for Cabo da Roca, EV for Évora, GR for Granada and MA for Madrid.

atmosphere. An estimation of the aerosol radiative forcing and forcing efficiencies are also provided. A detailed description of the version 2 AERONET inversion products is given by Holben et al. (2001). Table 1 shows the six AERONET stations distributed in the IP that were considered in this study: Barcelona (BA), Burjassot (BU), Cabo de Roca (CR), Évora (EV), Granada (GR) and Madrid (MA).

2.2. EARLINET lidars in the IP

The European Aerosol Research Lidar Network, EARLINET, included in the European Research Infrastructure for the observation of Aerosol, Clouds and Trace Gases (ACTRIS), aims at creating a quantitative, comprehensive, and statistically significant database for the horizontal, vertical, and temporal distribution of aerosols on a continental scale, providing the most extensive collection of ground-based data for the aerosol vertical distribution over Europe (Pappalardo et al., 2014). In this work four Iberian EARLINET stations (BA, MA, EV and GR) provided lidar data, all of them equipped with multi-wavelength lidars and some of them with depolarization capabilities (see Table 1). Burjassot lidar station was not available at this moment.

The EARLINET protocol establishes that lidar measurements have to be carried out on a regular basis: on Monday (at 14 UTC and at sunset) and on Thursday (sunset). Under exceptional events, as the one described in this work, EARLINET stations are encouraged to perform additional measurements in order to monitor the event over the longest period of time possible. During the period of 20–23 February 2017, EARLINET lidar measurements over the IP were performed as reported in Table 1. A temporal averaging of the profiles of 30 to 60 min was performed depending on the measurement duration available in order to guarantee a proper signal-to-noise ratio throughout the vertical column. Vertically resolved particle coefficients were derived by means of the Klett-Fernald algorithm (Klett, 1981; Fernald, 1984). This algorithm requires an assumption of the lidar ratio (LR), defined as the ratio of the particle extinction (α) to the particle backscatter (β) coefficient. We have used a generic value of 50 sr which can be considered a typical value of mineral dust (Guerrero-Rascado et al., 2008, 2009; Müller et al., 2009, 2010; Preissler et al., 2011). Whenever possible during nighttime, α and β coefficient profiles were retrieved independently with the Raman algorithm (Ansmann et al., 1992), which in turn allows computing the vertically-resolved lidar ratios. The benefit of Raman, multi-wavelength lidar products is that they provide some intensive parameters, such as the lidar ratio and the Ångström exponent, useful for the analysis of aerosol optical properties. The Ångström exponent (Ångström, 1964) is inversely related to the size of the particles: the greater the exponent, the smaller the particles and vice versa (Amiridis et al., 2009). The Ångström exponent, $AE(\lambda_1, \lambda_2)$, of a quantity α is defined for the wavelength pair (λ_1, λ_2) as:

$$AE(\lambda_1, \lambda_2) = -\frac{\log\left(\frac{\alpha(\lambda_1)}{\alpha(\lambda_2)}\right)}{\log\left(\frac{\lambda_1}{\lambda_2}\right)} \quad (1)$$

The Ångström exponent can be calculated for both the extinction and the backscatter coefficients. Whenever Raman, multi-wavelength inversions were available, the extinction Ångström exponent, AE, was calculated. The backscatter Ångström exponent, $\beta - AE$, was calculated for all inversions. Lidar systems equipped with depolarization channels (BA, EV and GR) also provided the aerosol volume and particle depolarization ratio and thus relevant information about the aerosol shape.

With regard to the errors associated to the measurements, we made use of the Monte-Carlo technique to estimate the uncertainties of the vertically-resolved backscatter and extinction coefficients. This technique is based on the random extraction of new lidar signals, where each bin is considered a sample element of a given probability distribution with the experimentally observed mean value and standard deviation. The extracted lidar signals are then processed with the same algorithm to obtain a set of solutions from which the standard deviation

is inferred as a function of height (Pappalardo et al., 2004). These statistical errors appear as error bars in the lidar-derived profiles of the backscatter and extinction coefficients.

2.3. Description of the models evaluated and methodology

The present analysis utilizes the operational 72-h dust forecasts of the BSC-DREAM8b (Pérez et al., 2006; Basart et al., 2012) and the NMMB/BSC-Dust (Pérez et al., 2011) models (http://www.bsc.es/ess/information/bsc-dust-daily-forecast) for the period from 19 to 22 February 2017. Both models are developed and operated at the Barcelona Supercomputing Center (BSC) and they are the two models considered for the development of the near-real time (NRT) evaluation within the Sand and Dust Storm Warning Advisory and Assessment System (SDS-WAS) Regional Center (https://sds-was.aemet.es/projects-research/evaluation-of-model-derived-dust-vertical-profiles). The NRT evaluation consists in comparing the modeled dust optical thickness to the observed total AOD provided by AERONET Version 3 and 2, Level 1.5 data. The Ångström exponent calculated between the wavelength pair (440, 870 nm) is used to distinguish the situations in which mineral dust is the dominant aerosol type. Threshold discrimination is made by discarding observations with an Ångström exponent higher than 0.6. Table 2 summarizes the main parameters used in the configuration of the models.

The modeled dust extinction values at 550 nm are directly compared with the observed particle extinction values at 532 nm because of the wavelength proximity and the low spectral extinction dependence of mineral dust (see Section 4). In order to have continuous observations and to maximize their number, day and nighttime inversions of particle backscatter coefficients are used and converted to extinction using a constant lidar ratio of 50 sr, a value validated later in Section 4. The vertical resolution of both dust models is much coarser than the lidar vertical resolution. In order to evaluate the models' capability to reproduce the vertical distribution of the dust extinction coefficient, the original lidar vertical resolution is downgraded to the resolution of the modeled profiles.

Given that the extinction value at a given height, h_i, of the models is the average extinction of the layer comprised between $h_i - \frac{h_i - h_{i-1}}{2}$ and $h_i + \frac{h_{i+1} - h_i}{2}$, the extinction value of the lidar profile at height h_i is calculated as the mean value of the original lidar profile (at the lidar original vertical resolution) calculated in the exact same layer of each model. For the horizontal resolution, the lidar data can be considered as point observations, while the models represent uniform pixels of 0.33° resolution (~33 km). The temporal resolution is also different: while the models provide instantaneous profiles with time steps of 3 h, the lidar profiles are averaged over 30 or 60 min. Here we have compared each modeled profile at time t with a 30- (60-) min. Averaged lidar-derived profile included in the interval [t − 30, t + 29 min.] ([t − 60, t + 59 min.]). In case two consecutive measurements fulfil this criterion, the measurement which was running at time t is selected. The forecast skill analysis is performed in terms of two vertically integrated statistical indicators, namely the fractional bias (*FB*), and the correlation coefficient (r), as well as in terms of the center of mass (CoM). *FB* and r are both calculated for the extinction coefficient. The fractional bias is a normalized measure of the mean bias and indicates only systematic errors, which lead to an under/overestimation of the estimated values. The linear correlation coefficient is a measure of the models' capability to reproduce the shape of the aerosol profile. The vertical integration is made from the lowest pair of simultaneously available model and observed values up to 6 km. No lower limit was fixed because of the dust plume proximity to the ground surface. The upper limit was fixed to 6 km because nearly no dust was detected above that height. The CoM was approximated by the particle backscatter weighted altitude as defined in Mona et al. (2006) who noted that this approximation "exactly coincides with the true center of mass if both composition and size distribution of the particles are constant with the altitude".

In Section 5 we evaluate the model performances for forecasts of 24 h (Section 5.1) and then we compare these forecasts to longer ones of 48 and 72 h (Section 5.2) to see how the forecast skill behaves as the lead time increases. A forecast (or a lead time) of 24 h represents all forecasts in the range [0; 23 h] since the model initialization. 48 and 72 h forecasts represent all forecasts in the range [24; 47 h] and [48; 71 h] since the model initialization, respectively.

3. Synoptic situation, columnar properties and singularity of the event

3.1. Synoptic situation

During the period from 20 to 23 February 2017, the synoptic situation in the IP was dominated by the influence of an anticyclone centered northwest from the Western coast, extending in ridge to South Central Europe and by the existence of a low pressure system, initially centered over Morocco, as illustrated in the European Centre for Medium-Range Weather Forecasts (ECMWF) ERA5 reanalysis of the Geopotential height at 850 hPa at several hours (Fig. 1). This low is very likely to be associated to a Sharav cyclone (Alpert and Ziv, 1989). The plots presented in Fig. 1 also include the surface wind friction velocity (u_*), which is a good indicator of possible dust emissions from deserts (Alfaro and Gomes, 2001; Darmenova et al., 2009 and references therein). It is generally assumed that the dust flux from the surface involves a power law of the wind friction velocity, as well as some parameters that characterize the surface, as the fraction of vegetation, the surface roughness and the soil texture and water content. Significant dust emissions are likely to occur for high friction velocities (above 0.6 m s^{-1}), presenting lower sensitivity to land surface parameters (Darmenova et al., 2009).

The Geopotential field at 850 hPa (Fig. 1) indicates the persistence of an atmospheric flow advecting air from the central North Africa (Algeria) crossing the IP. On 20 February strong friction velocity values ($>$ 6 m s^{-1}) over Algerian Sahara (Fig. 1a), a major dust source region (Ginoux et al., 2012), are suitable to force dust aerosol emissions (Darmenova et al., 2009). The well-shaped deep low, centered over central Morocco transported air from Algeria to southern Spain. Over the Central and Northern parts of the Peninsula, the dominant wind brought air from central Europe under the anticyclonic circulation. Wind vectors at 850 hPa are not represented in Fig. 1 for the sake of clarity, though at this level it is reasonable to assume geostrophic wind. The situation maintains very similar in the next day and on the 22 February the low provokes high winds on the western side (central-northern Algeria), which may be seen by the proximity of the isopleths and by the strong values of the friction velocity (Fig. 1c), which indicates strong dust emissions. On 23 February the northward shift of the Moroccan low originated weak precipitation events in several locations

Table 2
Main parameters of the dust models used in this study.

	BSC-DREAM8b	NMMB/BSC-Dust
Meteorological driver	Eta/NCEP	NMMB/NCEP
Model domain	North Africa-Middle East-Europe (25° W – 60° E and 0° – 65° N)	
Initial and boundary conditions	NCEP/GFS data (at 0.5° × 0.5° horizontal resolution) at 12 UT are used as initial conditions and boundary conditions at intervals of 6 h	
Horizontal resolution	0.33° x 0.33°	
Vertical resolution	24 Eta-layers	40 σ-hybrid layers
Time step	3 h	
Dust size bins	8 (0.1–10 μm)	
Radiation interactions	Yes	
Dust initial condition	24 h forecast from the previous day's model run	

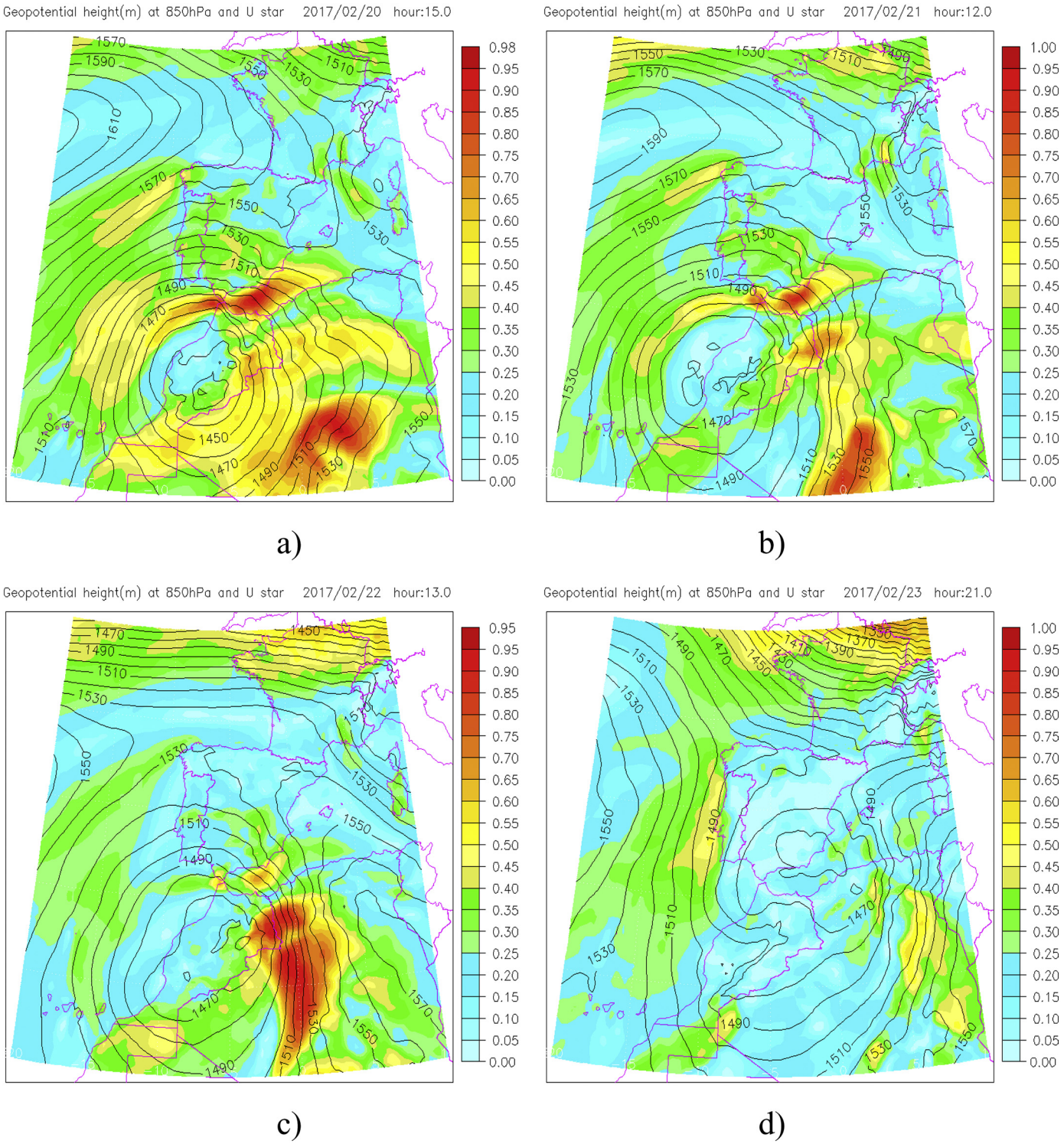

Fig. 1. ECMWF ERA5 reanalysis of the Geopotential height at 850 hPa (black height contours) and surface wind friction velocity (color bar in ms^{-1}) from 20 to 23 February 2017. Generated using Copernicus Atmosphere Monitoring Service information (CAMS, 2018). (For interpretation of the references to color in this figure legend, the reader is referred to the web version of this article.)

in the south of Portugal and Spain, but still transporting air from Algeria to Northeast Spain (Catalonia). The friction velocity over the desert regions dropped significantly, hinting at the end of the significant dust emissions. The synoptic conditions changed radically on 24 February with the passage of a frontal system that affected all the IP (not shown in Fig. 1).

Fig. 2 presents RGB composites based upon the combination of infrared channels (8.7, 10.8 and 12.0 μm) from the Spinning Enhanced Visible and InfraRed Imager (SEVIRI) on board Meteosat-10, showing the dust transport evolution (magenta) from 20 to 24 February 2017. The dust was transported across the Alboran Sea (western Mediterranean Sea) and infiltrated in southern Iberian atmosphere on 20 February (Fig. 2a), gradually transported towards west and north by the synoptic circulation, affecting the southern and western sites (CR, EV, GR) as illustrated by Fig. 2b and c. On the 22 February the dust intrusion was reinforced by a thick plume that progressively entered the

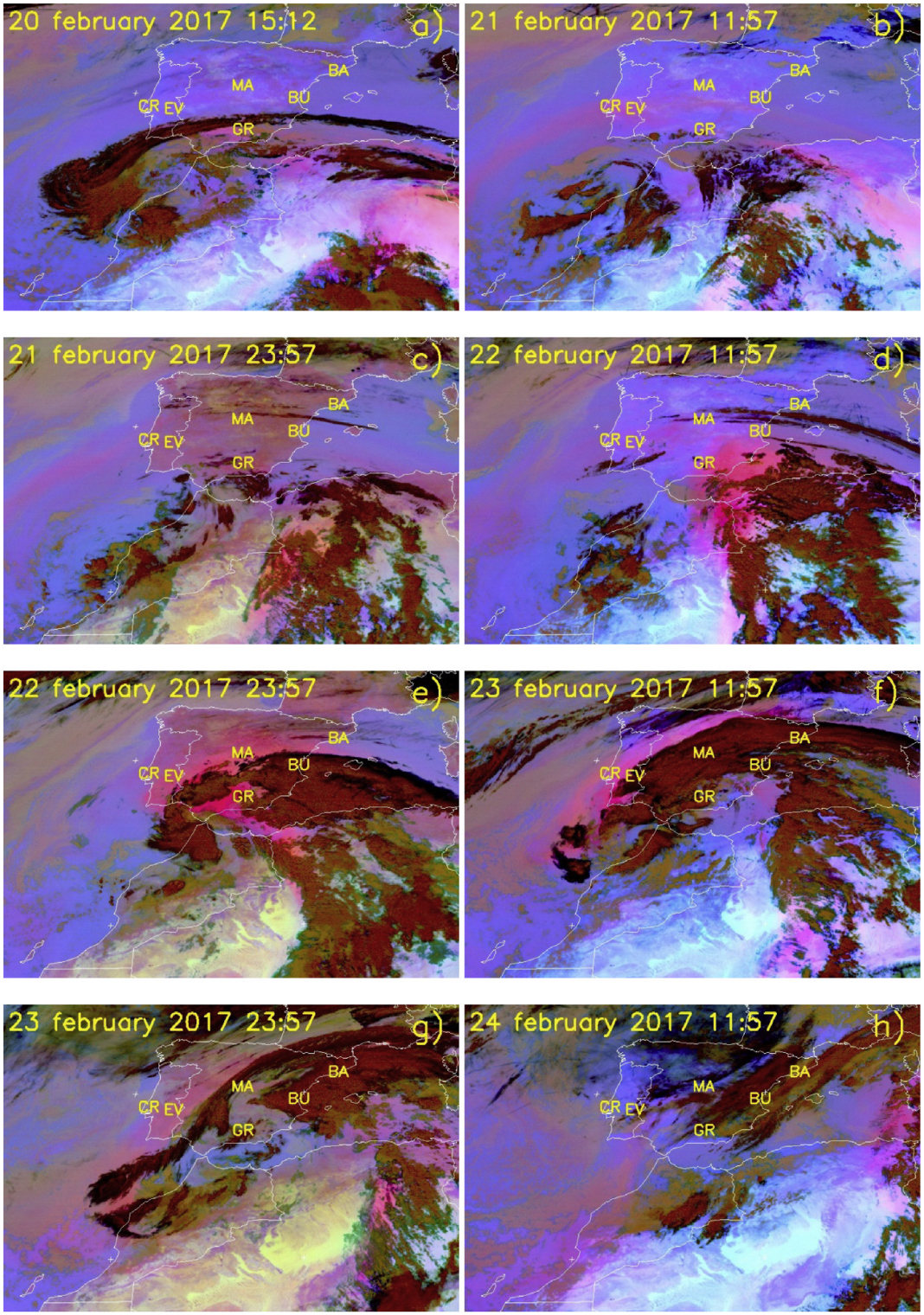

Fig. 2. Meteosat RGB composites showing the evolution of the dust plume from 20 to 24 February 2017. The Iberian sites considered in the study are also represented in the images: Barcelona (BA), Burjassot (BU), Cabo da Roca (CR), Évora (EV), Granada (GR) and Madrid (MA).

IP through the southeastern coast (Fig. 2d) extending north and westwards and affecting all sites represented in the images (Fig. 2e). This new intrusion was accompanied by the presence of high clouds that on the 23 February affected most of the IP, associated with the intensification and northward shift of the Moroccan low (Fig. 2f and g). The arrival of a frontal system from northwest on the 24 February interrupted the North African dust flow, pushing it towards the central Mediterranean regions (Fig. 2h).

The temporal evolution of the back-trajectories, from 20 to 24 February 2017, arriving over the six sites considered, at three atmospheric levels (2000, 3000 and 4000 m agl) is represented in the supplementary material in Fig. S1. The back-trajectories were calculated using the Hybrid Single-Particle Lagrangian Integrated Trajectory (HYSPLIT) model (Stein et al., 2015; Rolph et al., 2017), available

online at http://ready.arl.noaa.gov/HYSPLIT.php. The sequence shows that the first sites overpassed by air masses originating in northern Africa were: Granada (20 February; Fig. S1a), followed by Évora and Cabo da Roca (21 February; Fig. S1b and S1c). Burjassot and Madrid sites started to be influenced by North African air masses between the 21 and 22 February (Fig. S1d and S1e) and finally also Barcelona remained under the influence of the same air masses between the 23 and 24 February (Fig. S1f to S1h). Information from Meteosat RGB composites (Fig. 2) displaying the dust distribution over North African regions and back-trajectories (Fig. S1), hint at dust originating from central Algeria, where also strong values of wind friction velocities were found (Fig. 1).

3.2. Columnar properties

The desert dust plume entered the IP from the South on the 20 February, and then it gradually reached the northwest and later on the eastern part of the IP. Fig. 3 shows the time series data of AOD at 675 nm, Ångström exponent (440 and 870 nm) and SSA at 675 nm from 20 to 25 February 2017 in six sites distributed across the IP. An increase of the AOD was first noticed in Granada site on the 20 February, where the AOD values reach about 1.5, accompanied by very low values of AE, typical of desert dust intrusions, which is confirmed by the Meteosat composite in Fig. 2a. The dust plume maintains its influence over Granada and extends towards the western part of the IP, affecting in the next day also Évora and Cabo da Roca sites, with AOD values ranging between about 0.6 and 1.2, once again with very low AE (< 0.2). The dust transport continues and on the 22 February, during daytime, desert dust is detected in all stations except for Barcelona where it is measured on the next day. Still on the 22 February, extremely high AOD values are reached in Granada and Burjassot (> 2.0) and moderately high in Madrid, Évora and Cabo da Roca (0.5 < AOD < 1.0), with AE values lower than 0.2 for all these stations. The columnar size distribution (not shown) on 22 February shows a clear 3-mode distribution at Évora, Granada and Burjassot, with a coarse mode mean radius between 1.7 and 2.3 μm and a peak of the coarse mode volume concentration of

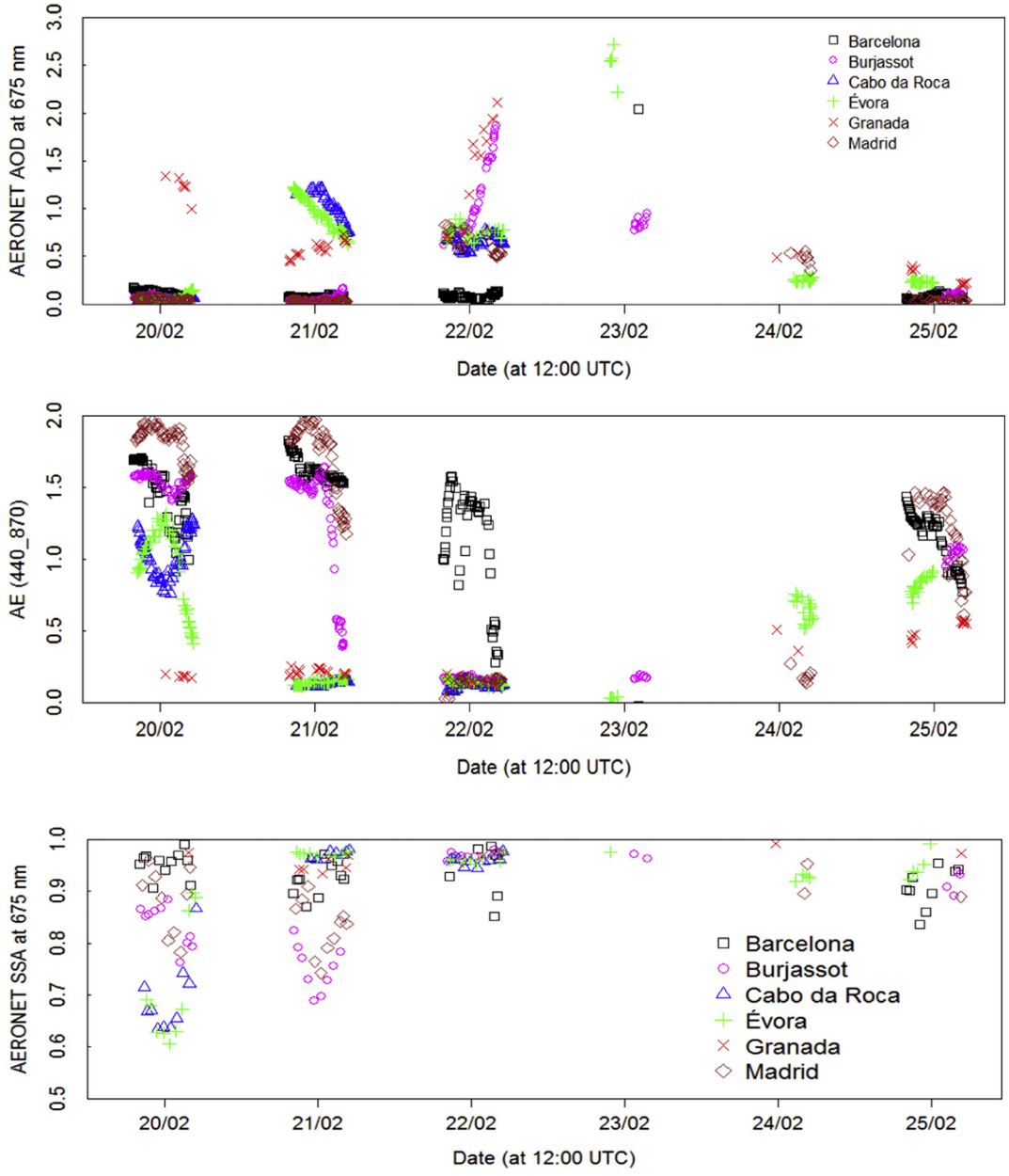

Fig. 3. AERONET AOD at 675 nm, AE (440 and 870 nm) and SSA at 675 nm from 20 to 25 February 2017 in six sites distributed across the IP.

$1\ \mu m^3\ \mu m^{-2}$ reached in the afternoon.

On the 23 February there are only a few AERONET measurements available due to the persistence of clouds over the region; nevertheless the AOD is still considerably high (> 2.0) at Évora and Barcelona with corresponding AE values around zero indicating the presence of air masses from desert dust source regions supported by the back-trajectories presented in the supplementary material (Fig. S1). As mentioned before, the frontal system on the 24 February interrupted the dust transport and the AOD values on the 24 and 25 February show a consistent decrease at all sites with a corresponding increase of the AE.

The single scattering albedo is characterized by relatively high values in all the stations during the dust event, showing the predominant dispersive nature of these particles. The lower SSA values (greater absorption) in the first two days in some of the sites (BU, CR, EV, MA) depicted in Fig. 3 are related with polluted air masses coming from northwestern Europe (not shown here).

3.3. Singularity of the dust event

The dust transport analyzed here regards a record-breaking episode that hit the Iberian Peninsula (IP) from 20 to 23 February 2017. According to AERONET (2019), this dust intrusion was the strongest over the IP since July 2012 and it is the strongest event (in terms of AOD) ever recorded over the IP during the month of February. It is noteworthy to mention that the AOD at 675 nm was > 2 in several AERONET stations and, during the most intense periods, some lidar and sun-photometer retrievals could not be performed due to high aerosol load, respectively, attenuating the lidar signal and blocking the sun. A

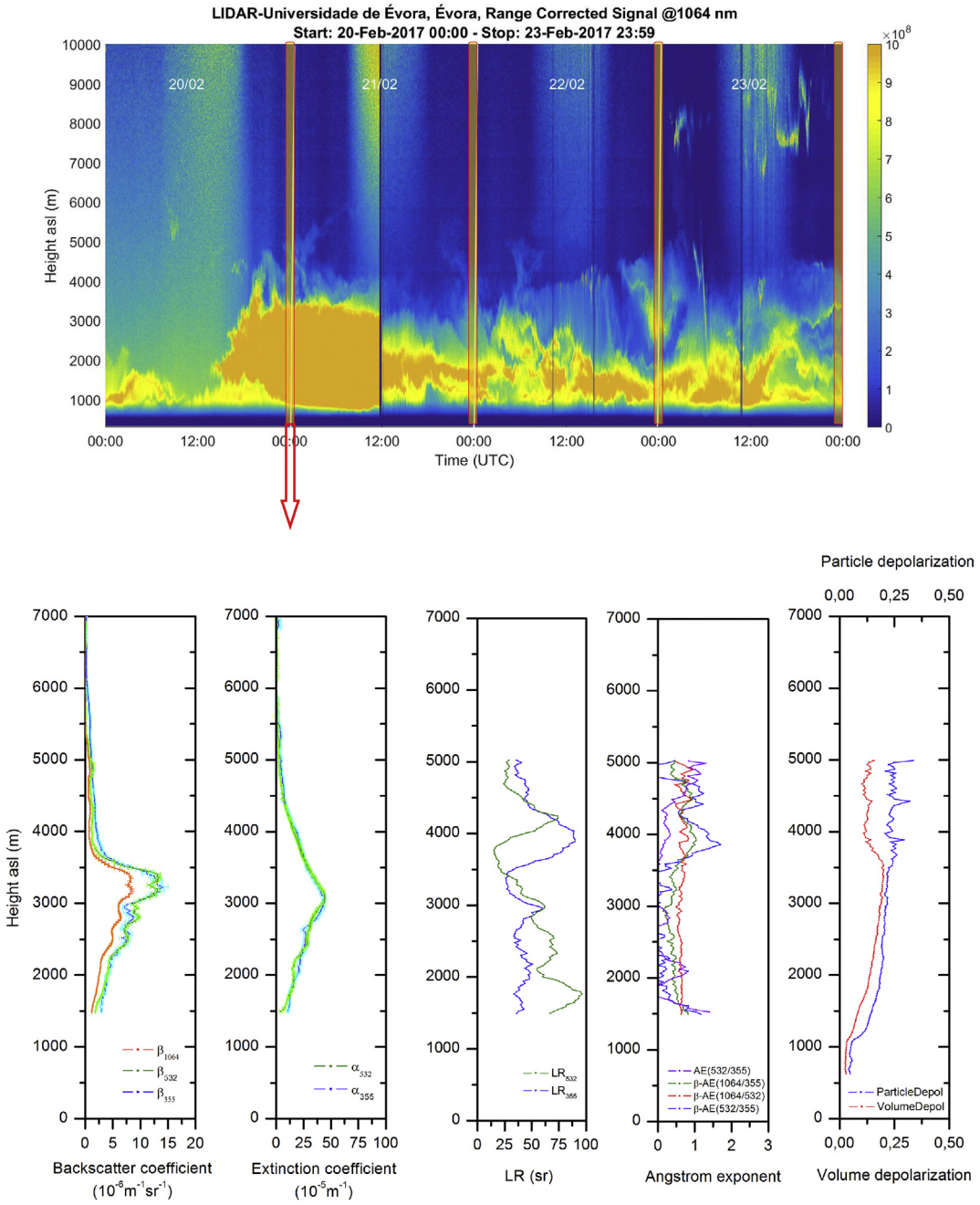

Fig. 4. (top) RCS at 1064 nm on 20–23 February 2017 at Évora (293 m asl); (bottom) Backscatter coefficient, extinction coefficient, Lidar ratio, Ångström exponents, and volume and particle depolarization ratio on 21 February 2017 at 00:00 UTC.

previous work concerning such events at the IP found AODs at 500 nm up to 1.5 in the south of Spain (Guerrero-Rascado et al., 2009), with maximum values of particle backscatter coefficients (15·Mm^{-1} sr^{-1} at 355 nm) similar to those registered during this event, however that event took place in September. Preissler et al. (2011) reported an aerosol optical thickness up to 2 in Portugal as a consequence of another extreme dust intrusion episode in April (Preissler et al., 2011).

Winter is the season when these phenomena are less likely to occur across the whole Mediterranean basin (Querol et al., 2009). However, extreme dust intrusions, as the one described in this paper or others that took place quite recently (Cazorla et al., 2017; Sorribas et al., 2017), occurred during the coldest season.

AERONET data presented in the supplementary material in Figs. S2 to S4 and Table S1 illustrate the exceptionality of this event in the region. Figs. S2 (and S3) show the density scatter plots of the AE (440–870) versus the AOT at 675 nm, using all available AERONET level 1.5 (level 2.0) data for each of the stations considered in the study. The black dots superimposed in these plots illustrate the values measured during the February 2017 desert dust intrusion. It can be noted that the event is positioned in a tail of the data group with very low AE accompanied by high AOT values. When quality-assured AERONET data is considered (Fig. S3), the event under study is characterized by the highest AOT values in almost all stations, except for Cabo da Roca and Madrid where these values are still very high and near the maxima.

Fig. S4 of the supplementary material shows percentile plots of AOT at 675 nm and AE (440–870) using all available Level 1.5 AERONET data, as well as the data corresponding to the event under study (black dots). Table S1 presents percentiles of AOT at 675 nm and AE (440–870), as well as a characterization of the desert dust based on the AOT at 550 nm following Gkikas et al. (2013). According to the fifth IPCC (2013) report, an extreme weather event can be defined as a rare phenomenon taking into account its historical statistical distribution for a particular place and/or time. Then 10th and 90th percentiles are usually considered as reference to define “rare”. As shown in Fig. S4, all AOT values measured during the February 2017 desert dust event are above the 90th percentile; simultaneously, all AE (440–870) values are below the 10th percentile, which in conformity with IPCC allows affirming that this was a rare event. Additionally, the methodology proposed by Gkikas et al. (2013) was applied and results are shown in the third table of Table S1. The mean AOT at 550 nm during the event, at each of the considered AERONET sites, was always greater than Mean + 4 x Std, which allows to define the episode as extreme. This is important to be highlighted as extreme weather events have been discussed and suggested to be connected to climate change. For instance some remaining questions concern whether or not such events take place earlier or later in the season or if their severity has been increased (WMO, 2011).

4. Vertically-resolved optical properties

4.1. Situation in Évora

Fig. 4 represents the temporal evolution of the Range Corrected Signal (RCS) during 4 days which provides a very detailed overview of the phenomenon, as well as a lidar inversion at a selected time. To note that on 21 February (12:00 UTC) a change of the neutral-density filters in front of the detection channel was necessary to be carried out in order to attenuate the received light. This obviously reduced the RCS at this point but did not affect the retrieval of aerosol optical properties. Four different periods have been selected so as to analyze aerosol optical properties from the African plume observed in Évora (highlighted in red in the top plot of Fig. 4). Nighttime measurements have been chosen for the analysis in order to estimate accurately such properties given the fact that independent extinction from Raman signals was available at this lidar station. The first period (21st Feb from 0:00–0:30 UTC) presents the highest backscatter coefficient values out of all periods evaluated, so a special attention has been paid to this period (bottom plot of Fig. 4). Notwithstanding the other 3 periods are also analyzed and results are shown in the supplementary material Figs. S5, S6 and S7. Mean aerosol optical properties are reported in Table 3 for specific atmospheric layers in which the dust plume is representative. During the first period analyzed (21st Feb from 0:00–0:30 UTC, bottom plot of Fig. 4) the African dust plume is detected up to 5 km height asl with a peak of the particle backscatter coefficient at 3.2 km asl. In the layer between 1.5 and 3.5 km asl, the layer-averaged values of the backscatter-related Ångström exponent at the wavelength pairs 532/355, 1064/532 and 1064/355 are 0.08 ± 0.33, 0.62 ± 0.04 and 0.42 ± 0.13, respectively. The extinction-related Ångström exponent at 532/355 nm is 0.16 ± 0.45. These small values are typical for dust as previously reported during extreme African dust intrusions (Guerrero-Rascado et al., 2009; Preissler et al., 2011; Mamouri et al., 2016). The other periods, except on 23 Feb. at 00:00 UTC, also show relatively low backscatter- and extinction-related Ångström exponent values. The relative high value on 23 Feb. at 00:00 UTC (β-AE between the pairs 1064/532–1.28) is probably due to artefacts from the optical inversions. On 23 Feb. around noon the highest aerosol load was recorded in Évora (AOD ~ 2.5). The signal attenuation on the lidar measurement was very strong and may have hampered the correct

Table 3
Summary of mean aerosol optical properties retrieved from Raman and elastic lidar measurements in Évora and in Granada for 4 selected periods.

Atmospheric layer	LR_{355} (sr)	LR_{532} (sr)	β-AE 1064-532	β-AE 532-355	β-AE 1064-355	AE 532-355	δ-vol.	δ-part.
ÉVORA								
00:00 UTC-21Feb 1.5–3. km asl	40 ± 8	61 ± 18	0.62 ± 0.04	0.08 ± 0.33	0.42 ± 0.13	0.16 ± 0.45	0.16 ± 0.03	0.19 ± 0.02
00:00 UTC-22Feb 1.5–4 km asl	45 ± 4	38 ± 8	0.76 ± 0.12	−0.12 ± 0.23	0.44 ± 0.08	0.16 ± 0.19	0.16 ± 0.01	0.21 ± 0.01
00:00 UTC-23Feb 1.5–5 km asl	52 ± 7	40 ± 9	1.28 ± 0.33	−0.62 ± 0.48	0.58 ± 0.19	0.01 ± 0.27	0.16 ± 0.02	0.19 ± 0.01
23:39 UTC-23Feb 1.5–4. km asl	55 ± 12	34 ± 8	1.00 ± 0.18	−0.96 ± 0.29	0.28 ± 0.17	0.18 ± 0.24	0.12 ± 0.01	0.15 ± 0.01
GRANADA								
13:30 UTC-20Feb 2.0–4.0 km asl			0.27 ± 0.12	0.19 ± 0.30	0.24 ± 0.04		0.19 ± 0.03	0.22 ± 0.04
20:00 UTC-20Feb 1.8–4.0 km asl	52 ± 7	53 ± 6	0.19 ± 0.08	0.54 ± 0.21	0.32 ± 0.07	0.51 ± 0.43	0.20 ± 0.02	0.25 ± 0.03
07:31 UTC-21Feb 1.5–3.4 km asl			0.86 ± 0.07	0.64 ± 0.13	0.77 ± 0.08		0.18 ± 0.03	0.28 ± 0.01
12:30 UTC-22Feb 1.5–4.0 km asl			0.39 ± 0.12	0.32 ± 0.17	0.36 ± 0.07		0.26 ± 0.01	0.31 ± 0.02

retrieval of the Rayleigh signal above the dust layer. The same phenomenon is observed at other stations.

Since Raman signals were available and extinction coefficients were obtained independently, particle lidar ratios were derived as well. The dust layer located between 1.5 and 3.5 km asl on 21Feb (00:00 UTC) presented a lidar ratio of 40 ± 8 sr and 61 ± 18 sr at 355 and 532 nm, respectively. Our estimates at 355 nm are in agreement with Mona et al. (2006) who found a mean lidar ratio at 355 nm of 38 ± 15 sr for three years of Raman lidar measurements of Saharan dust in southern Italy. Conversely, lidar ratio at 532 nm is found greater than the lidar ratio at 355 nm for the first period analyzed (21 Feb, 00:00 UTC), which is not usual for dust particles as it has been already pointed out by other authors (Müller et al., 2010). Nevertheless, this trend is only observed in the first period analyzed, the other three analyzed periods show a lidar ratio at 532 lower than the lidar ratio at 355 nm. The reason behind this observation (high unexpected lidar ratio values at 532 nm) can be attributed to non-accurate retrievals hampered by the high aerosol load which produces a great extinction and consequently a decrease of the signal-to-noise ratio. It is noteworthy to mention that the standard deviation of the mean lidar ratio at 532 nm on 21Feb (00:00 UTC) is significantly higher compared to the rest of the studied period. The lidar ratio at 355 nm on 23 Feb (at 00:00 and 23:39 UTC) seems a bit higher than values reported in the literature (Mona et al., 2006) and it could be due to a decrease of the African dust intrusion intensity and therefore a greater proportion of local aerosol might be present in the atmosphere. The lidar ratio at 532 nm in all cases (apart from the first period) are consistent with literature since typical values range 35–45 sr for typical desert dust (Mamouri et al., 2013; Nisantzi et al., 2015; Mamouri et al., 2016). In addition, the volume and particle depolarization ratio were 0.16 ± 0.03 and 0.19 ± 0.02 for the aforementioned atmospheric layer on 21Feb 00:00 UTC. These two latter parameters are constant with altitude, which indicates that no change in the aerosol type is observed within the atmospheric layer of interest. They are also very similar for the four periods studied,

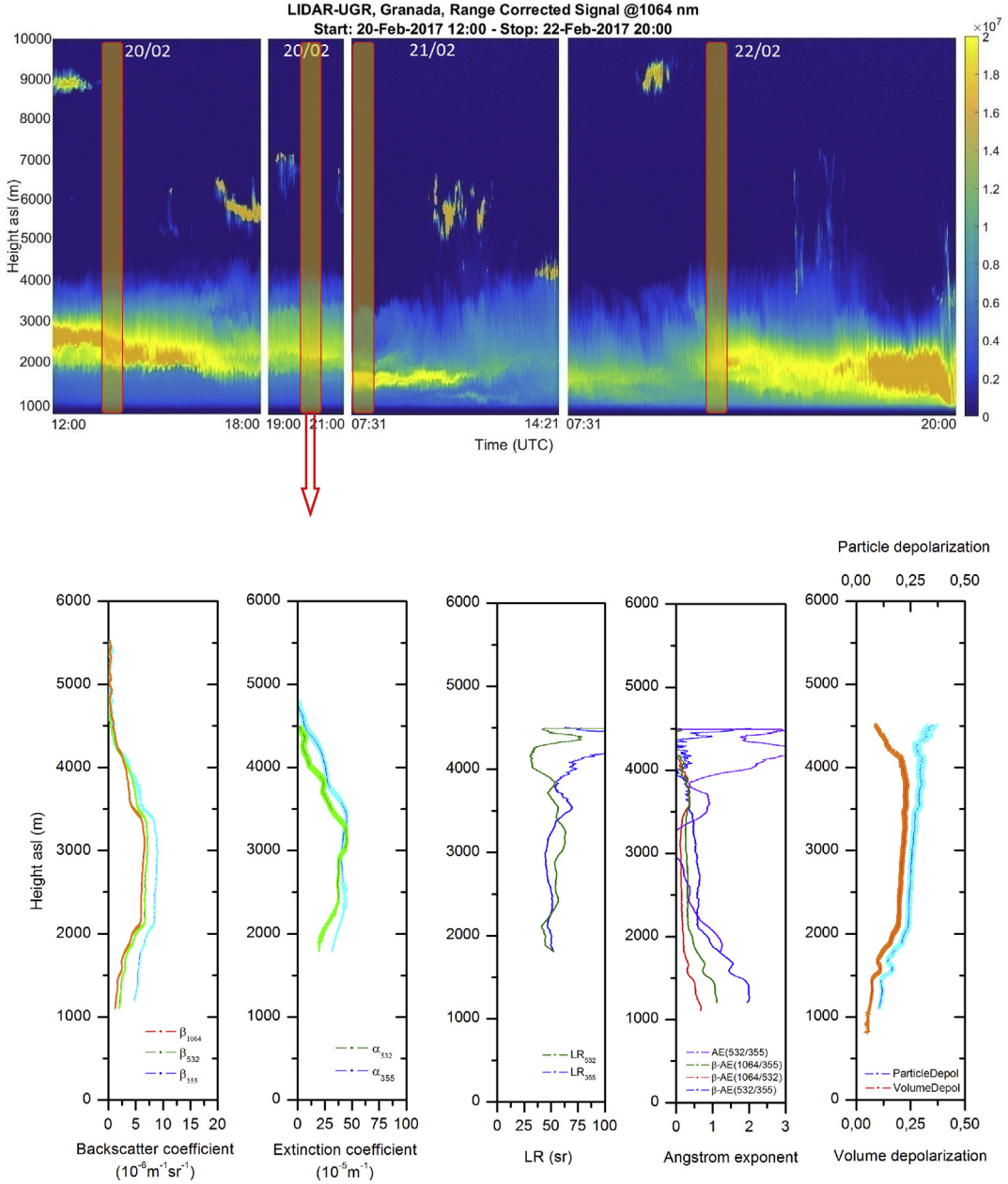

Fig. 5. (top) RCS at 1064 nm during four periods in the interval 20–23 February 2017 at Granada (680 m asl); (bottom) Backscatter coefficient, extinction coefficient, Lidar ratio, Ångström exponents, and volume and particle depolarization ratio on 20 February 2017 at 20:00 UTC.

however the last period indicates lower volume and particle depolarization values that is associated with the decrease of intensity of the Saharan dust intrusion and a greater contribution of local aerosols.

4.2. Situation in Granada

In Granada, lidar measurements were carried out during four periods of time during the extreme African dust intrusion: 12:00-18:00 and 19:00-21:00 UTC on 20 February, 07:31-14:21 UTC on 21 February, and 07:31-20:00 UTC on 22 February. Such measurements are represented in Fig. 5, as well as a lidar inversion at a selected night time. The red areas indicate the selected periods where vertically-resolved aerosol optical properties have been derived. Such vertical profiles can be seen in the bottom plot of Fig. 5 and in the supplementary material in Figs. S8, S9 and S10. For a better comprehension of these data, layer-averaged aerosol optical properties are also presented in Table 3. In general terms, the maximum altitude of the dust plume was registered at 4 km asl approximately and it maintained relatively constant throughout the four lidar measurements. For certain periods (13:30–14:21 UTC on 21st Feb) intensification of the RCS is observed at the top of the dust plume, which may indicate cloud formation processes related to mineral dust.

Concerning intensive aerosol optical properties, backscatter-related and extinction-related Ångström exponents were low, in accordance with previous lidar observations, which indicates a large aerosol size. The Raman retrieval could be performed only for the period 19:00-21:00 UTC on 20 February. On 22 February, the African dust intrusion was so intense that it produced large extinction and hampered proper retrieval. The lidar ratios obtained at Granada were 52 ± 7 and 53 ± 6 at 355 and 532 nm respectively. As far as volume and particle depolarization ratios are concerned, these parameters show similar and consistent values to data obtained in the Évora station. Nevertheless, it is noteworthy to mention that the last analyzed period (12:30 UTC on 22nd Feb) exhibits the greatest volume (0.26 ± 0.01) and particle

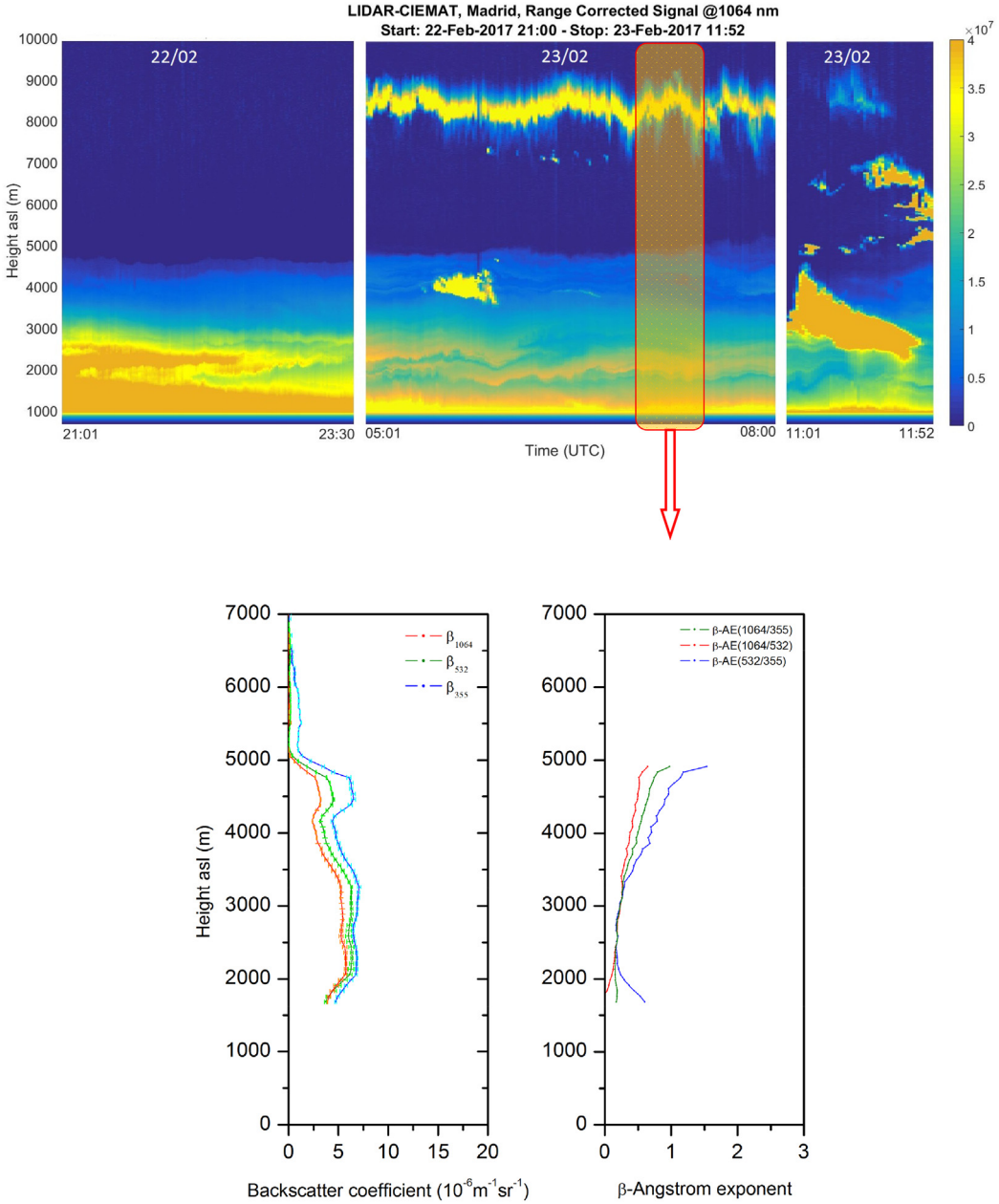

Fig. 6. (top) RCS at 1064 nm during three periods in the interval 22–23 February 2017 at Madrid (669 m asl); (bottom) Backscatter coefficient and backscatter-related Ångström exponents on 23 February 2017 at 06:59 UTC.

(0.31 ± 0.02) depolarization ratios observed in all lidar stations. This value of the particle depolarization ratio (0.31) is representative of pure mineral dust (fine and coarse mode) (Mamouri and Ansmann, 2014).

4.3. Situation in Madrid

In Madrid the African dust plume was only detected in the last stage of the African event (from 22 February on) when the dust intrusion was at its peak of intensity. Lidar measurements on 20 February (not shown) at Madrid still did not present any sign of this extraordinary plume. Three lidar measurement periods were available at this station: on 22 Feb (21:00-23:36 UTC) and 23 Feb (05:00-08:00 and 11:00-11:52 UTC). They are represented in Fig. 6. As it can be seen the thickness of the plume ranged from the ground to 5 km asl and in the last lidar measurement the plume was accompanied by thick clouds. Concerning the retrieval of vertically-resolved aerosol optical properties, only the period 05:00–08:00 UTC (23 Feb) was considered for this purpose. Such profiles are represented in the bottom plot of Fig. 6, which concerns the period 06:59–07:29 UTC. The signal attenuation observed on the first (due to dust) and third (due to dust and clouds) lidar measurement periods was again very strong, and in most cases the Rayleigh signal could not be reached with enough signal-to-noise ratio in order to properly retrieve the aerosol optical properties. This is a problem that needs to be highlighted in this study as it appeared in several lidar stations: the dust load was so strong that at the peak of the event it had the same effect on lidar signals than clouds have in terms of signal attenuation.

Finally, the bottom plot of Fig. 6 presents 3 backscatter coefficient

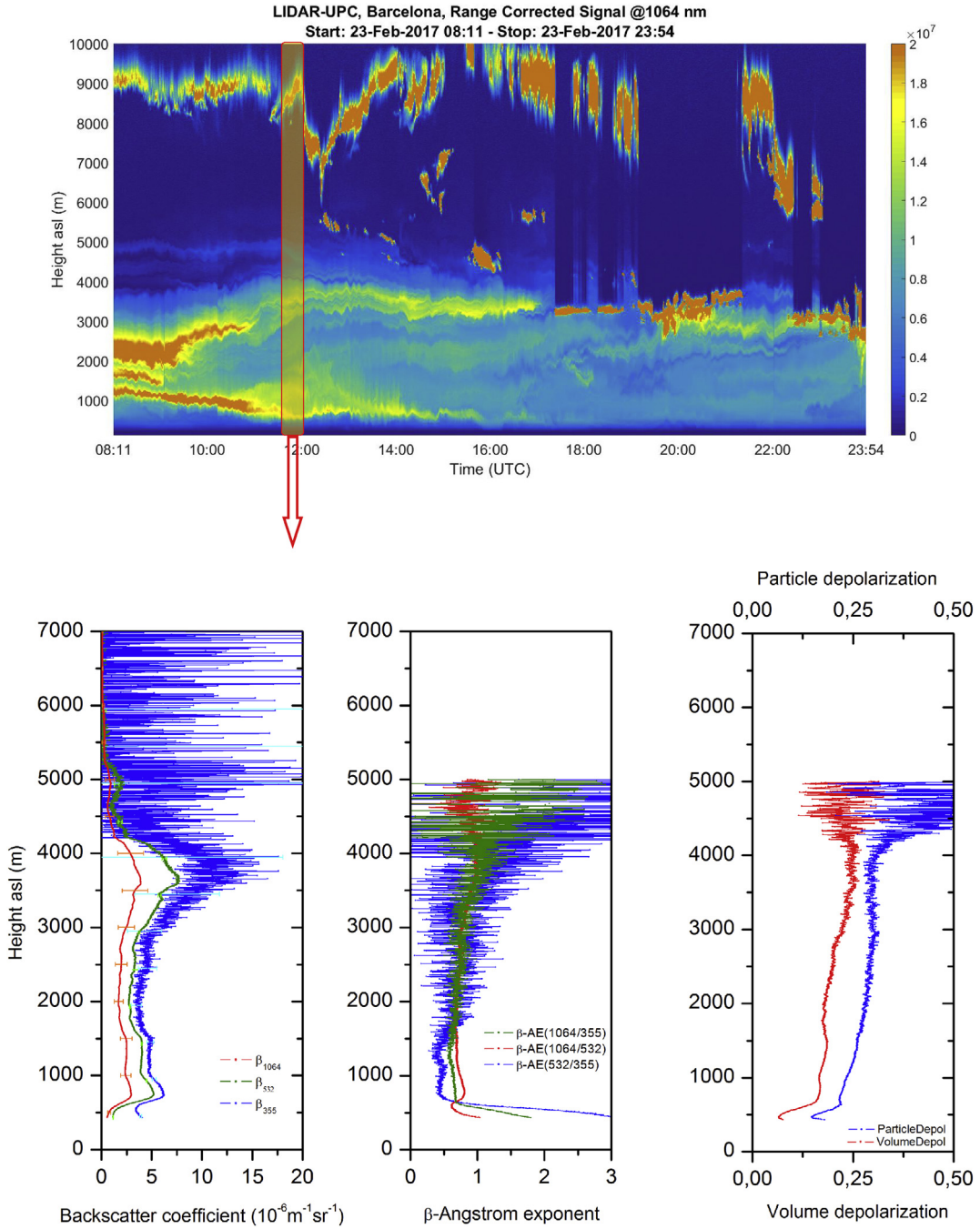

Fig. 7. (top) RCS at 1064 nm on 23 February 2017 at Barcelona (115 m asl); (bottom) Backscatter coefficient, backscatter-related Ångström exponents and volume and particle depolarization ratios on 23 February 2017 at 11:34 UTC.

profiles at 1064, 532 and 355 nm and their respective backscatter-related Ångström exponents. No particle extinction coefficients could be obtained independently as Raman signal were too noisy due to the aforementioned reasons. Maximum values of particle backscatter coefficient are reached at 2.2–2.3 km asl. At this altitude β_{355} is 6.85 ± 0.09, β_{532} is 6.35 ± 0.13 and β_{1064} is 5.75 ± 0.01 $Mm^{-1}\,sr^{-1}$. Mean backscatter-related Ångström exponents were found to be 0.52 ± 0.34, 0.28 ± 0.17, 0.37 ± 0.22 at the wavelength pairs: 532/355, 1064/532 and 1064/355 nm for the atmospheric layer established from lidar full overlap height to 4.9 km. These low backscatter-related Ångström exponents are in accordance with previous lidar observations, which partially indicate a large aerosol size.

4.4. Situation in Barcelona

According to the meteorological overview, the Barcelona site was the latest place from the time standpoint that was hit by the extreme African dust intrusion. As it can be seen in Fig. 7 the African dust plume was registered throughout almost the entire 23 February. At the beginning of the lidar measurement (from 08:11 to 12:00 UTC), the maximum altitude of the plume was detected at 5 km asl approximately and after that it decreased gradually until it reached the value of 3–3.5 km at 23:54 UTC. One period of 30 min has been selected at 11:34 UTC to show the retrieval of aerosol optical properties from the lidar measurement (bottom plot of Fig. 7). The reason to choose this period lies on the availability of a clear atmosphere to derive Rayleigh extinction. As indicated by the color code, the RCS was considerably high for the atmospheric layer between 1 and 3 km before 11:00 UTC. From 11:00 UTC onward the RCS intensity decreases and the dust layer structure is a bit different than in the morning. It must also be noted that from 12:00 UTC on the aerosol optical properties retrieval is quite complex since it is quite difficult to detect a clean atmospheric layer so as to derive the Rayleigh extinction, which is mandatory to infer the aforementioned aerosol optical properties. For the period 12:00–16:00 UTC dispersed clouds can be observed at 5–7 km and from 17:00 UTC

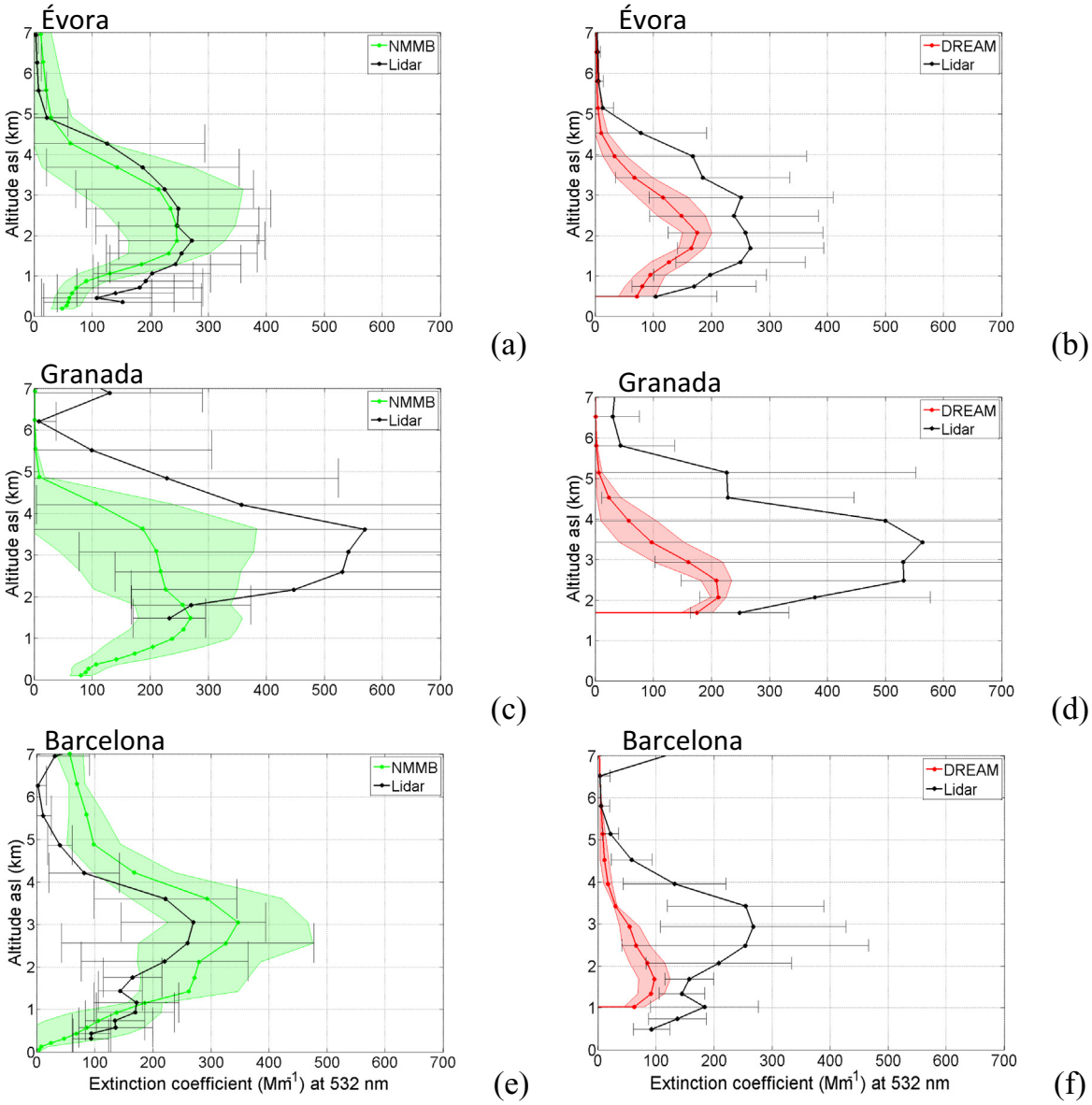

Fig. 8. Mean vertical distribution of mineral dust extinction coefficient estimated by NMMB/BSC-Dust in (a) Évora, (c) Granada and (e) Barcelona and by BSC-DREAM8b in (b) Évora, (d) Granada and (f) Barcelona. The period considered, not always continuous, are 21 Feb. 12UT – 23 Feb. 23UT, 21 Feb. 12UT – 22 Feb. 19UT and 23 Feb. 08UT – 23 Feb. 21UT for Évora, Granada and Barcelona, respectively. The model shaded areas and the error bars of the lidar represent the standard deviations. All model forecasts are for a lead time of 24 h.

onward clouds are registered at the top of the dust plume layer (at 3.5–4 km), which prevents the Rayleigh extinction computation. This latter observation is also interesting from the point of view of cloud formation processes. Considering the evolution of the plume throughout the entire lidar measurement at 4 km, it is plausible that African dust aerosol might act as cloud condensation nuclei (see how the RCS at 4 km from 18:00 to 23:54 UTC becomes more intense than earlier during the day).

The bottom plot of Fig. 7 shows aerosol optical properties obtained for the period 11:34-12:04 UTC. While the backscatter coefficient values are comparable to the ones observed in Madrid, the backscatter-related Ångström exponents seem to be higher in Barcelona. In Barcelona below 1.7 km asl the Ångström exponents are below 1 and have a non-negligible spectral dependence, and above 1.7 km asl they are very similar and nearly constant at 0.7–0.8. Volume and particle depolarization ratios for the atmospheric layer situated at 1–3 km asl are similar than in the previous period. The mean values are 0.19 ± 0.01 and 0.28 ± 0.02 respectively.

5. Performance of dust models during extreme events

This section aims at examining the performance of dust models to predict the 3D evolution of mineral dust during such intense intrusions. The literature available on the evaluation of modeled dust vertical profiles usually inspects the behavior of such models on long time series or for a single moderate intrusion (Gobbi et al., 2013; Santos et al., 2013; Mona et al., 2014; Binietoglou et al., 2015; Sicard et al., 2015), and only rarely for intense intrusions (Huneeus et al., 2016; Ansmann et al., 2017; Tsekeri et al., 2017).

The results are presented for the three sites of Évora, Granada and Barcelona. There are too few measured profiles in Madrid to allow for a statistical comparison. The lidar-derived profiles of extinction coefficient were retrieved as explained in Section 2.3. As it has been observed on the plots of the backscatter coefficients (Figs. 4–7) the error associated to the backscatter coefficient is rather small, so that the error on the extinction is driven by the variability of the lidar ratio which according to Table 3 is on the order of 25%. As a comparison, Córdoba-Jabonero et al. (2018) calculated the error on the extinction coefficient using the same methodology but applied to elastic MPL systems and found errors associated to the extinction on the order of 15–40%.

Before looking at the vertical distribution we briefly discuss the models horizontal transport by comparing Fig. S11 which shows BSC-DREAM8b and NMMB/BSC-Dust forecast of dust optical thickness to the maps of Meteosat (Fig. 2) on the same dates and times. The first result is that both models predict a similar horizontal distribution of the dust although BSC-DREAM8b predicts a much less intense event and seems to depict horizontal structures with less details than NMMB/BSC-Dust does. When comparing to Meteosat images, the agreement of NMMB/BSC-Dust is relatively good. On 23 Feb. at 00 and 12UT the shape and position of the dust cloud with respect to the IP is very well captured by NMMB/BSC-Dust although it may be displaced a little towards the northwest compared to the satellite observations. Towards the end of the event both models seem to predict the persistence of dust off the coast of Morocco while the observations show that the dust cloud has moved northeast.

5.1. Forecast skill for a lead time of 24 h

The comparison of the temporal mean profiles of extinction coefficient is made for NMMB/BSC-Dust and BSC-DREAM8b in Fig. 8. The temporal means are averaged over the whole period (see caption of Fig. 8). For each individual profile the correlation coefficient is plotted as a function of fractional bias (FB) in Fig. 9 and the temporal evolution of the latter two parameters is shown in Fig. 10. In the latter figure the time evolution of *FB* and *r* is also shown for lead times of 48 and 72 h and discussed in Section 5.2. The mean values of the fractional bias, the correlation coefficient and the center of mass for both models at each site are reported in Table 4. Table 4 also contains these mean values for lead times of 48 and 72 h, which are discussed in Section 5.2.

When looking at the temporal mean profiles of extinction coefficient (Fig. 8), the most striking feature is the general large underestimation of BSC-DREAM8b at all heights independently of the site. This underestimation is smaller in Évora (mean $FB = -57.3$ %, Table 4) than in Granada (mean $FB = -95.0$ %) and Barcelona (mean $FB = -93.8$ %), where the underestimation is larger. In Fig. 9 we observe a horizontal spread of the variability of *FB* larger in Évora ([−115; +65%]) than in Granada ([−150; −20%]) and Barcelona ([−130; −30%]) probably due to the smaller amount of vertical profiles available at both sites. The same tendency is observed on NMMB/

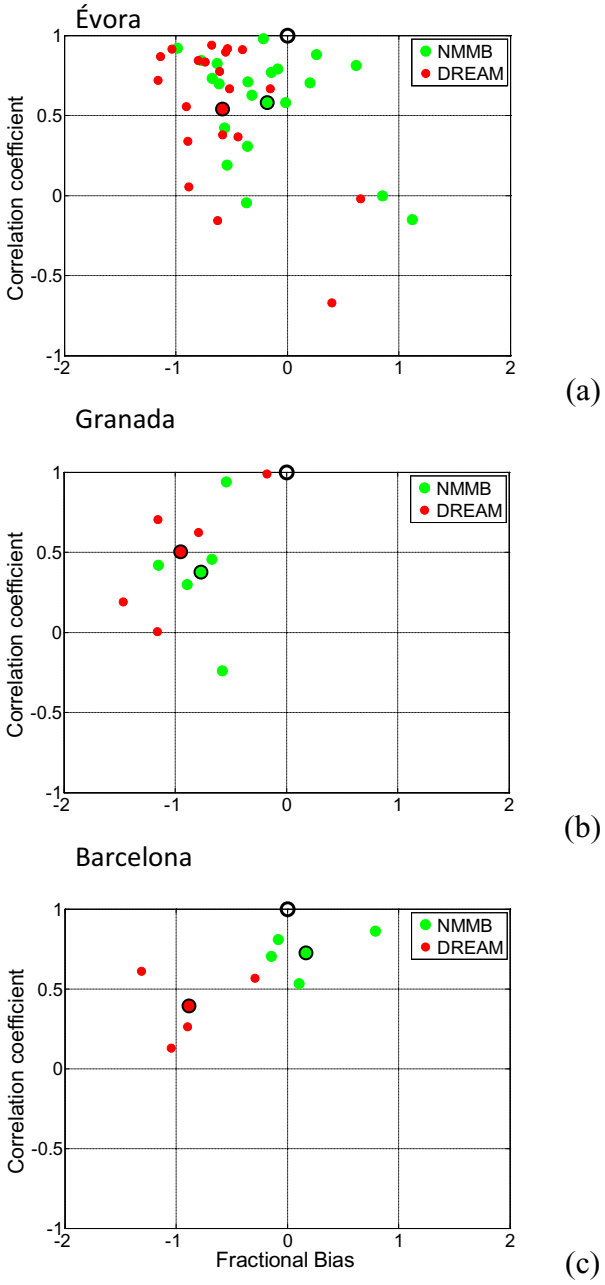

Fig. 9. Correlation coefficient vs. fractional bias, both calculated for the extinction coefficient, calculated for each individual profile in (a) Évora, (b) Granada and (c) Barcelona. All model forecasts are for a lead time of 24 h. The mean values are represented by larger dots edged by a black line. The ideal (*FB*/*r*) pair, (0/1), is indicated by a black circle.

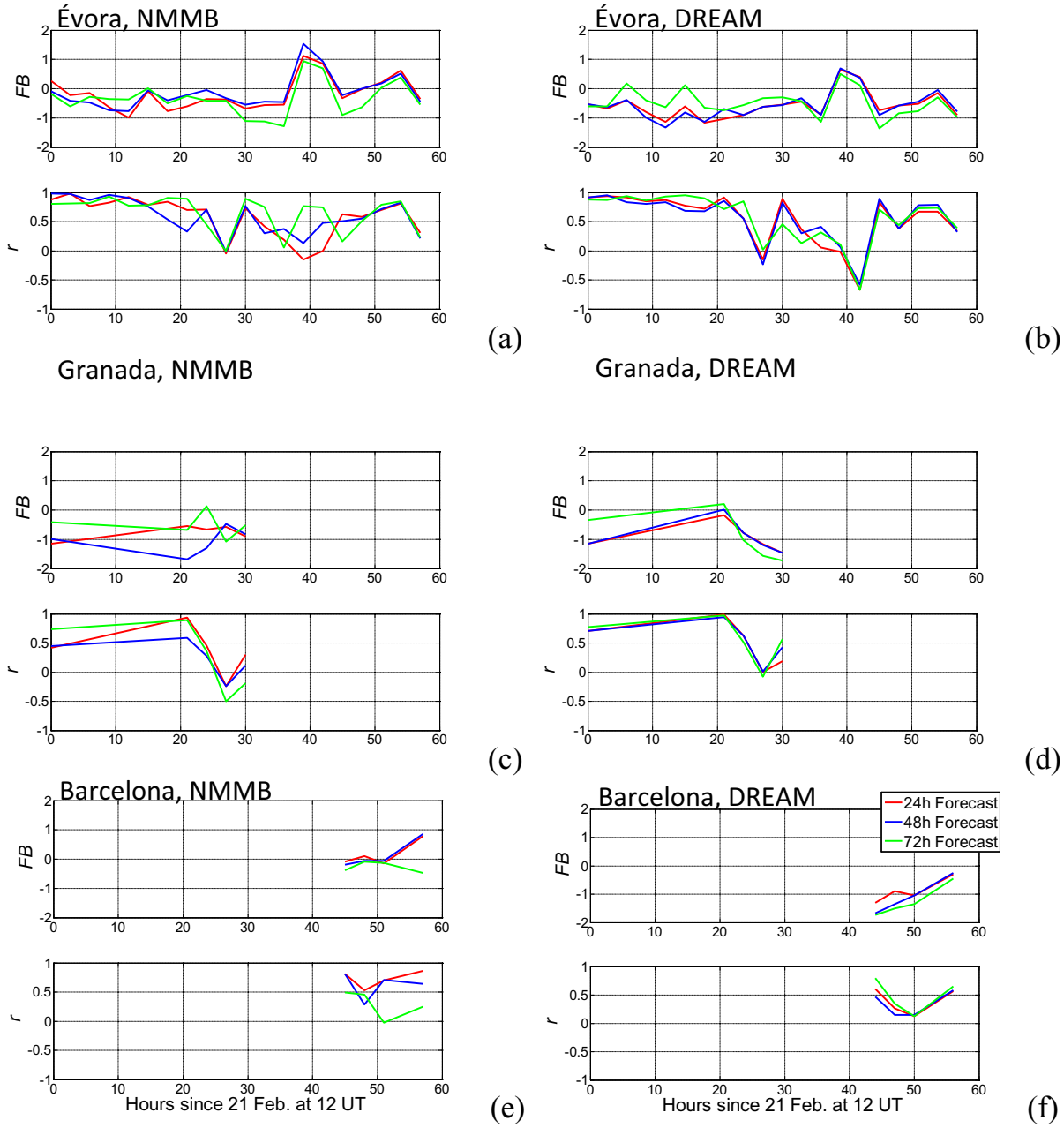

Fig. 10. Correlation coefficient and fractional bias, both calculated for the extinction coefficient, vs. time for forecast lead times of 24, 48 and 72 h for NMMB/BSC-Dust in (a) Évora, (c) Granada and (e) Barcelona and for BSC-DREAM8b in (b) Évora, (d) Granada and (f) Barcelona. The legend shown in the last plot applies to all plots.

BSC-Dust data. NMMB/BSC-Dust forecasts show a rather good agreement with the observations, especially in Évora and in Barcelona. While the model tends to underestimate the observations in Évora (especially below the CoM; the mean *FB* is −20.5%) and in Granada (especially near the CoM; the mean *FB* is −72.6%), it tends to overestimate the observations in Barcelona (especially above 1 km; the mean *FB* is +16.6%). The agreement between NMMB/BSC-Dust and the Évora lidar is remarkably good (Fig. 13a), taking into account the atmospheric variability represented by the lidar error bars and the rather long period considered (60 h). While the NMMB/BSC-Dust profiles reach zero at an approximate height of 5 km in Évora and Granada (similarly to the observations), the profiles in Barcelona start decreasing linearly from ~100 Mm^{-1} at 5 km height to ~50 Mm^{-1} at 7 km (when the observations indicate an extinction coefficient lower than 50 Mm^{-1} above 4.5 km and reaching zero at 6 km). The increase of the lidar profile at 7 km is due to the presence of a cloud above 7 km (see Fig. 7) taken into account in the computation of the layer-average lidar extinction coefficient at the model height. Possible explanations of the differences observed between NMMB/BSC-Dust and the observation in Barcelona in the upper part of the profile are given in the next paragraph. Also in Barcelona the lidar profiles show a layer connected to the surface below 1.5 km, which is not reproduced by either of the models. The main reason is probably the presence of non-dust type particles mixed with the dust detected in the observations but not taken into account in the models. It is also worth noting that BSC-DREAM8b reproduces less atmospheric variability than NMMB/BSC-Dust (in Fig. 8, the red shaded areas are smaller than the green ones), whereas the atmospheric variability denoted by the lidar error bars is large at all sites. This seems to indicate that BSC-DREAM8b has lower vertical variability in comparison to NMMB/BSC-Dust.

Table 4
Main results of the comparison between models and observations. *FB* and *r* are both calculated for the extinction coefficient.

	Évora (21 Feb. 12UT – 23 Feb. 23UT)					
	NMMB/BSC-Dust			BSC-DREAM8b		
Number of profiles	20					
Lead time (hours)	24	48	72	24	48	72
FB (%)	−20.5	−11.1	−35.7	−57.3	−57.0	−47.9
r	0.56	0.57	0.61	0.54	0.55	0.57
Model CoM (km)	2.70	2.82	3.04	2.21	2.26	2.38
Lidar CoM (km)	2.73			2.47		
	Granada (21 Feb. 12UT – 22 Feb. 19UT)					
	NMMB/BSC-Dust			BSC-DREAM8b		
Number of profiles	5					
Lead time (hours)	24	48	72	24	48	72
FB (%)	−72.6	−98.4	−46.9	−95.0	−91.5	−89.0
r	0.37	0.21	0.25	0.49	0.53	0.54
Model CoM (km)	2.26	2.38	2.14	2.70	2.79	2.95
Lidar CoM (km)	3.31			3.38		
	Barcelona (23 Feb. 08UT – 23 Feb. 21UT)					
	NMMB/BSC-Dust			BSC-DREAM8b		
Number of profiles	4					
Lead time (hours)	24	48	72	24	48	72
FB (%)	+16.6	+13.6	−27.0	−93.8	−112.8	−131.4
r	0.72	0.60	0.30	0.36	0.31	0.46
Model CoM (km)	3.61	3.72	4.37	2.51	2.53	2.69
Lidar CoM (km)	2.57			2.59		

The capacity of the models to reproduce the shape of the dust vertical distribution is estimated with the correlation coefficient calculated between individual modeled and observed profiles. NMMB/BSC-Dust seems to perform better in Barcelona (*r* values of 0.72) and in Évora (0.56) than in Granada (0.37). BSC-DREAM8b seems to perform better in Évora (*r* values of 0.54) and in Granada (0.49) than in Barcelona (0.36). The low *r* value obtained with BSC-DREAM8b in Barcelona (0.36) is apparently due to a vertical downward transport forecast by the model and not visible from the observations (the peak of BSC-DREAM8b profile is approximately 2 km lower than the peak of the lidar, see Fig. 8f). Huneeus et al. (2016) who compared NMMB/BSC-Dust and BSC-DREAM8b, among other models, to CALIOP (Cloud Aerosol Lidar with Orthogonal Polarization) profiles during an intense dust intrusion in April 2011 with an AOD ~ 0.8, found a general underestimation of the dust layer height, that was attributed to an overestimation of the dust deposition near the source. Wet scavenging is another source of uncertainty in dust forecast models. As mentioned in Section 3.1 this event was associated to a convective cell giving some precipitation over North Algeria and Southern Iberian Peninsula. These severe convective events have associated more uncertainty in the predicted weather fields (e.g. amount of precipitation) and consequently in the dust prediction. This is directly linked with the removal of dust from the atmosphere and to the aerosol lifetime in the upper layers. The fact that the cloud of points along the *r*-axis is more spread in Évora (Fig. 9a) than in Granada or Barcelona (Fig. 9b and c) is probably due to the longer time series available in Évora covering two and a half days of the event. Another indicator of the score of the models related to the vertical structure of the dust layer is the center of mass. In Évora both models retrieve well the center of mass of the dust layers (differences between modeled and observed CoM are < 0.21 km, see Table 4). In Granada, both models reproduce smaller CoM values with discrepancies vs. the observations of 1.05 km (NMMB/BSC-Dust) and 0.68 km (BSC-DREAM8b). At this site both models predict a center of mass of the dust plume closer to the ground than it is in reality. In Barcelona BSC-DREAM8b predicts well the CoM with a discrepancy of 0.06 km, The overall performance of BSC-DREAM8b at all three stations are in relatively good agreement with the difference of 0.3 ± 1.0 km found between the same model and the EARLINET station of Potenza, Italy, over a period of 12 years and for dust events with AOD < 0.9 (Mona et al., 2014). In Barcelona, the mean CoM forecasted by NMMB/BSC-Dust is 3.61 km while the lidar measured a mean value of 2.57 km. This large difference is due to the mean NMMB/BSC-Dust profile of extinction in Barcelona which does not reach zero at ~5 km, unlike at the other sites (Fig. 8e; see also the former paragraph). This finding suggests that one or several processes taken into account in NMMB/BSC-Dust and inducing vertical motion of the dust layers did actually not occur. In our case the vertical upward transport of the dust layers at high altitudes forecast in Barcelona but not in the southern sites is probably due to a too long aerosol lifetime in the upper layers and/or underestimated deposition processes (Mona et al., 2014). Interestingly this overestimation of NMMB/BSC-Dust in the upper layers was also observed by Binietoglou et al. (2015) who found a slight overestimation of NNMB/BSC-Dust above 4.5–5 km when comparing the model with LIRIC (Lidar/Radiometer Inversion Code) profiles of mass concentration at several sites in Europe and by Sicard et al. (2015) who compared the model with profiles from EARLINET stations during a moderate dust event affecting the western Mediterranean Basin in July 2012.

5.2. Forecast skill temporal evolution and comparison for different lead times

The temporal evolution of the score of the models (in terms of *FB* and *r*) for different lead times shown in Fig. 10 allows us to evaluate the forecast skill of each model as a function of time since the forecast initialization. The start of the time series is fixed on 21 February 2017, at 12 UTC, referred in the following as time T_0, when the first observations are available (in Évora and Granada). The observations available allow us to have 20 points of comparison (at a 3-h time step)

from the 21st at 12 UTC until the 23rd at 23 UTC in Évora; 5 points of comparison on the 22nd between 07 and 19 UTC in Granada; and 4 points of comparison on the 23rd between 08 and 21 UTC in Barcelona. In all plots we have represented the temporal evolution of *FB* and *r* for lead times of 24, 48 and 72 h. We first discuss the forecast skill temporal evolution for a lead time of 24 h, and then compare it to the evolution at 48 and 72 h.

In Évora during the first 20 h (Fig. 10a and b, red lines) both models have similar and more or less stable correlation coefficients with values larger than 0.5. The fractional bias is negative and varies in the range [−100; 0%]. It is larger (in absolute value) for BSC-DREAM8b than for NNMB/BSC-Dust. At T_0 + 20 hours (the 22nd at 08 UTC) the situation starts to degrade: *FB* variations are larger from one prognostic to the next, especially for NNMB/BSC-Dust, and *r* passes regularly below the value of 0.5. A few hours before T_0 + 40 hours (the 23rd at 04 UTC) and only for a period of 5–6 h both models overestimate the extinction coefficient ($+50 < FB < +150$ %). During the first hours of the 23rd the AOD in Évora reached its highest values (~2.5; see Fig. 3). In that sense, it seems that the peak of the event is well reproduced in time by the models but its intensity is overestimated. In Granada (Fig. 10c and d, red lines) the prognostic of NNMB/BSC-Dust is quantitatively better (smaller values of *FB*) but qualitatively worst (smaller correlation coefficients) than for BSC-DREAM8b. Our findings in Granada are in the same line as those found by Sicard et al. (2015) for a moderate dust event affecting the western Mediterranean Basin in July 2012 who also found that NNMB/BSC-Dust reproduced quantitatively better the profiles while BSC-DREAM8b reproduced better the shape of the profiles. The decrease of *FB* visible for both models in Granada and starting at T_0 + 20 (the 22nd at 08 UTC) coincides with the increase of AOD from ~0.5 to values above 2.0 (see Fig. 3). While on the peak day in Évora (the 23rd) both prognostics show an overestimation for a short period of time, on the peak day in Granada (the 22nd) the general underestimation of both prognostics is accentuated, especially for BSC-DREAM8b. In Barcelona (Fig. 10e and f, red lines) the comparison starts at T_0 + 44 (the 23rd at 08 UTC) at the peak of the event in Barcelona (AOD > 2.0, see Fig. 3). NNMB/BSC-Dust shows a very good quantitative agreement in the morning and an overestimation in the afternoon, while BSC-DREAM8b shows an underestimation, which decreases with time. The shape of the vertical profiles is better reproduced by NNMB/BSC-Dust ($r > 0.5$) than by BSC-DREAM8b ($r < 0.5$). In general the forecast skills of BSC-DREAM8b in Barcelona are not as good as those of the southernmost sites. This difference, also observed by Huneeus et al. (2016) for dust northward transport, might be explained by the difficulties of the models in simulating horizontal winds and vertical dust propagation.

If we now look at the forecast skill as a function of lead time, i.e. at the differences between the red, blue and green lines in Fig. 10, corresponding, respectively, to lead times of 24, 48 and 72 h, the most striking result is that, at first sight, no clear degradation of the prognostics is clearly visible. There is a difference in the temporal evolution of the prognostics: the prognostics at 24 and 48 h are usually quite similar and the one at 72 h is the one that differs the most from the prognostic at 24 h. Nevertheless, the overall mean values in Table 4 do not show any clear tendency neither in terms of *FB*, nor *r*, for Évora and Granada, the two stations closest to the source. In this sense these results are in agreement with those of Huneeus et al. (2016) who found that the forecast skill of both models for AOD was independent of the forecasting lead time in the domain they defined as southern Europe. In Barcelona a slight degradation of the model scores occurs with increasing lead times: the fractional bias increases (in absolute value; BSC-DREAM8b) and the correlation coefficient decreases (NMMB/BSC-Dust) between the prognostics at 24 and 72 h. This deterioration of the forecast skills is not observed in Huneeus et al. (2016) and may be due to the singularity and exceptionality of the event described in our study.

6. Conclusions

An extreme dust intrusion transported from Northern Africa to the western Mediterranean during 20–23 February 2017 has been reported and analyzed in the IP. By means of lidar and sun-photometer measurements, we have provided a representative picture of this extreme event by means of a detailed 4-D characterization of aerosol optical properties and their evolution during the dust intrusion. Furthermore, the combined use of active and passive remote sensing instruments along with dust models has provided useful information to better understand the complexity of dust long-range transport, its extreme character and also the capability of dust models to forecast such events.

The synoptic conditions that led to such an extreme event are the combination of a Moroccan low and the Atlantic anticyclonic system which were responsible for the tropospheric flow that advected mineral dust over the IP. According to AERONET sites over the IP, the aerosol optical depth at 675 nm peaked at values larger than 2.0 with associated Ångström Exponents (440–870 nm) close to 0 and single scattering albedos close to 1. On the most intense days of the event (22 and 23 February) the high load of atmospheric mineral dust blocked the sun and prevented quality-assured AERONET AOD inversions. Towards the end of the event (23 February) clouds started to form on top of the dust layer.

EARLINET/ACTRIS lidar measurements confirmed the presence of atmospheric dust in all stations (EV, GR, MA and BA). In general, the dust plume was observed between the ground until 4–5 km asl approximately. Maximum values of backscatter coefficients at 532 nm were registered in the range 10–15·Mm^{-1} sr^{-1}. Like for the AERONET sun-photometer, during the most intense period of the event the dust attenuation was such that the lidar signal-to-noise ratio in the molecular region above the dust layer was not high enough to perform reliable inversions. Backscatter-related Ångström exponents were monitored very close to 0. Lidar ratios were found in the range 40–55 sr at 355 nm and 34–61 sr at 532 nm during the event at Évora and Granada. Particle depolarization ratios, registered at those stations where depolarizing channels were available (EV, GR and BA), have revealed to be rather constant in the dust layer. Mean particle depolarization ratios in the dust layer of 0.19 were observed at the beginning of the event (20–21 February, Évora) and up to 0.31 at the peak of the event (22 February, Granada; 23 February, Barcelona).

The study also focused on the ability of the dust forecast models to reproduce the arrival, the vertical distribution and the intensity of the dust plume over a long-range transport region. The two dust models considered are the ones currently in development for the NRT evaluation within the SDS-WAS Regional Center: BSC-DREAM8b and NMMB/BSC-Dust. In general, the models' performances are highly dependent on the type of event and the region. Therefore, from a single event, we cannot conclude that one model is better than the other. However, and in the particular case of the February 2017 dust event, we found a large underestimation in the forecast of the extinction coefficient provided by BSC-DREAM8b at all heights independently of the site. In contrast NMMB/BSC-Dust forecasts presented a better agreement with the observations, especially in Évora. However NMMB/BSC-Dust reproduced a higher atmospheric variability than BSC-DREAM8b. Some discrepancies such as the forecast of dust by NMMB/BSC-Dust in layers well above 5 km are still not completely understood and further research is needed. Finally, with regard to the forecast skill as a function of lead time, no clear degradation of the prognostic is appreciated at 24, 48 and 72 h for Évora and Granada stations. However the prognostic does degrade (bias increases and/or correlation decreases) for Barcelona, which is attributed to the singularity of the event.

Acknowledgments

The research leading to these results has received funding from the H2020 program from the European Union (grant agreement no.

654109, 778349) and also from the Spanish Ministry of Industry, Economy and Competitiviness (MINECO, ref. CGL2013-45410-R, CGL2016-81092-R, CGL2017-85344-R, TEC2015-63832-P), the Spanish Ministry of Science, Innovation and Universities (ref. CGL2017-90884-REDT); the CommSensLab "Maria de Maeztu" Unity of Excellence (ref. MDM-2016-0600) financed by the Spanish Agencia Estatal de Investigación. Co-funding was also provided by the European Union through the European Regional Development Fund (ref. POCI-01-0145-FEDER-007690, ALT20-03-0145-FEDER-000004, ALT20-03-0145-FEDER-000011); by the Andalusia Regional Government (ref. P12-RNM-2409); by the Madrid Regional Government (projects TIGAS-CM, ref. Y2018/EMT-5177 and AIRTEC-CM, ref. P2018/EMT4329); by the University of Granada through “Plan Propio. Programa 9 Convocatoria 2013” and by the Portuguese Foundation for Science and Technology and national funding (ref. SFRH/BSAB/143164/2019). The BSC-DREAM8b and NNMB/BSC-Dust (now NMMB-MONARCH) model simulations were performed by the Mare Nostrum supercomputer hosted by the Barcelona Supercomputer Center (BSC). S. Basart acknowledges the AXA Research Fund for supporting aerosol research at the BSC through the AXA Chair on Sand and Dust Storms Fund, as well as the InDust project (COST Action CA16202). The authors gratefully acknowledge the NOAA Air Resources Laboratory (ARL) for the provision of the HYSPLIT transport and dispersion model and/or READY website (http://www.ready.noaa.gov) used in this publication.

Appendix A. Supplementary data

Supplementary data to this article can be found online at https://doi.org/10.1016/j.atmosres.2019.06.007.

References

AERONET (AErosol RObotic NETwork), https://aeronet.gsfc.nasa.gov/, last access: 13 March 2019.

Alfaro, S., Gomes, L., 2001. Modeling mineral aerosol production by wind erosion: Emission intensities and aerosol size distributions in source areas. J. Geophys. Res. 106 (D16), 18075–18078.

Alpert, P., Ziv, B., 1989. The Sharav Cyclone: Observations and some theoretical considerations. J. Geophys. Res. 94. https://doi.org/10.1029/88JD04228.

Amiridis, V., Balis, D., Giannakaki, E., Stohl, A., Kazadzis, S., Koukouli, M., Zanis, P., 2009. Optical characteristics of biomass burning aerosols over Southeastern Europe determined from UV-Raman lidar measurements. Atmos. Chem. Phys. 9 (7), 2431–2440.

Andreae, M., 1995. Climate effects of changing atmospheric aerosol levels. In: Henderson-Sellers, A. (Ed.), World Survey of Climatology, 16, Future Climate of the World. Elsevier, New York, pp. 341–392.

Ångström, A., 1964. The parameters of atmospheric turbidity. Tellus 16 (1), 64–75.

Ansmann, A., Wandinger, U., Riebesell, M., Weitkamp, C., Michaelis, W., 1992. Independent measurement of extinction and backscatter profiles in cirrus clouds by using a combined Raman elastic-backscatter lidar. Appl. Opt. 31 (33), 7113–7131.

Ansmann, A., Rittmeister, F., Engelmann, R., Basart, S., Jorba, O., Spyrou, C., Rémy, S., Skupin, A., Baars, H., Seifert, P., 2017. Profiling of Saharan dust from the Caribbean to western Africa–Part 2: Shipborne lidar measurements versus forecasts. Atmos. Chem. Phys. 17 (24), 14987–15006.

Basart, S., Perez, C., Nickovic, S., Cuevas, E., Baldasano, J., 2012. Development and evaluation of the BSC-DREAM8b dust regional model over Northern Africa, the Mediterranean and the Middle East. Tellus B 64.

Binietoglou, I., Basart, S., Alados-Arboledas, L., Amiridis, V., Argyrouli, A., Baars, H., Baldasano, J., Balis, D., Belegante, L., Bravo-Aranda, J., Burlizzi, P., Carrasco, V., Chaikovsky, A., Comeron, A., D'Amico, G., Filioglou, M., Granados-Munoz, M., Guerrero-Rascado, J., Ilic, L., Kokkalis, P., Maurizi, A., Mona, L., Monti, F., Munoz-Porcar, C., Nicolae, D., Papayannis, A., Pappalardo, G., Pejanovic, G., Pereira, S., Perrone, M., Pietruczuk, A., Posyniak, M., Rocadenbosch, F., Rodriguez-Gomez, A., Sicard, M., Siomos, N., Szkop, A., Terradellas, E., Tsekeri, A., Vukovic, A., Wandinger, U., Wagner, J., 2015. A methodology for investigating dust model performance using synergistic EARLINET/AERONET dust concentration retrievals. Atmos. Measure. Techniq. 8 (9), 3577–3600.

Boucher, O., Randall, D., Artaxo, P., Bretherton, C., Feingold, G., Forster, P., Kerminen, V.-M., Kondo, Y., Liao, H., Lohmann, U., Rasch, P., Satheesh, S.K., Sherwood, S., Stevens, B., Zhang, I.X.Y., Stocker, T.F., Qin, D., Plattner, G.-K., Tignor, A.M., Boschung, S.K., Nauels, J., Xia, A., Bex, Y., Midgley, P.M., 2013. Clouds and Aerosols. Climate Change 2013: The Physical Science Basis. Cambridge, United Kingdom and New York, NY, USA. pp. 571–657.

CAMS, Copernicus Atmosphere Monitoring Service Information, http://apps.ecmwf.int/datasets/data/cams-gfas/, last access: 18 May 2018.

Cazorla, A., Casquero-Vera, J.A., Román, R., Guerrero-Rascado, J.L., Toledano, C., Cachorro, V., Orza, J.A., Cancillo, M.L., Serrano, A., Titos, G., Pandolfi, M., Alastuey, A., Hanrieder, N., Alados-Arboledas, L., 2017. Near-real-time processing of a ceilometer network assisted with sun-photometer data: monitoring a dust outbreak over the Iberian Peninsula. Atmos. Chem. Phys. 17, 11861–11876.

Córdoba-Jabonero, C., Sicard, M., Ansmann, A., del Águila, A., Baars, H., 2018. Separation of the optical and mass features of particle components in different aerosol mixtures by using POLIPHON retrievals in synergy with continuous polarized Micro-Pulse Lidar (P-MPL) measurements. Atmos. Meas. Tech. 11, 4775–4795. https://doi.org/10.5194/amt-11-4775-2018.

Córdoba-Jabonero, C., Sicard, M., Basart, S., del Águila, A., Jiménez, M., Ramón Moreta, J., Zorzano, M.-P., 2019. An unusually extreme wintertime Saharan dust intrusion observed at two Spanish MPLNET sites: Performance of a dust model mass concentration profiles versus lidar observations. Atmos. Environ (in review).

Cuevas, E., Gómez-Peláez, A.J., Rodríguez, S., Terradellas, E., Basart, S., Garcia, R.D., Garcia, O.E., Alonso-Perez, S., 2017. The pulsating nature of large-scale Saharan dust transport as a result of interplays between mid-latitude Rossby waves and the North African Dipole Intensity. Atmos. Environ. 167, 586–602.

Darmenova, K., Sokolik, I.N., Shao, Y., Marticorena, B., Bergametti, G., 2009. Development of a physically-based dust emission module within the Weather Research and forecasting (WRF) model: Assessment of dust emission parameterizations and input parameters for source regions in Central and East Asia. J. Geophys. Res. 114, D14201.

Fernald, F.G., 1984. Analysis of Atmospheric Lidar Observations - some comments. Appl. Opt. 23 (5), 652–653.

Forster, P., Ramaswamy, V., Artaxo, P., Berntsen, T., Betts, R., Fahey, D., Haywood, J., Lean, J., Lowe, D., Myhre, G., Nganga, J., Prinn, G., Raga, G., Schulz, M., Van Dorland, R., 2007. Changes in Atmospheric Constituents and in Radiative Forcing. Climate Change 2007: The Physical Science Basis. Cambridge University Press, U.K, pp. 129–234.

Ginoux, P., Prospero, J.M., Gill, T.E., Hsu, N.C., Zhao, M., 2012. Global-scale attribution of anthropogenic and natural dust sources and their emission rates based on MODIS Deep Blue aerosol products. Rev. Geophys. 50.

Gkikas, A., Hatzianastassiou, N., Mihalopoulos, N., Katsoulis, V., Kazadzis, S., Pey, J., Querol, X., Torres, O., 2013. The regime of intense desert dust episodes in the Mediterranean based on contemporary satellite observations and ground measurements. Atmos. Chem. Phys. 13, 12135–12154. https://doi.org/10.5194/acp-13-12135-2013.

Gobbi, G., Angelini, F., Barnaba, F., Costabile, F., Baldasano, J., Basart, S., Sozzi, R., Bolignano, A., 2013. Changes in particulate matter physical properties during Saharan advections over Rome (Italy): a four-year study, 2001-2004. Atmos. Chem. Phys. 13 (15), 7395–7404.

Guerrero-Rascado, J., Ruiz, B., Alados-Arboledas, L., 2008. Multi-spectral Lidar characterization of the vertical structure of Saharan dust aerosol over southern Spain. Atmos. Environ. 42 (11), 2668–2681.

Guerrero-Rascado, J., Olmo, F., Aviles-Rodriguez, I., Navas-Guzman, F., Perez-Ramirez, D., Lyamani, H., Arboledas, L., 2009. Extreme Saharan dust event over the southern Iberian Peninsula in september 2007: active and passive remote sensing from surface and satellite. Atmos. Chem. Phys. 9 (21), 8453–8469.

Holben, B., Eck, T., Slutsker, I., Tanre, D., Buis, J., Setzer, A., Vermote, E., Reagan, J., Kaufman, Y., Nakajima, T., Lavenu, F., Jankowiak, I., Smirnov, A., 1998. AERONET - a federated instrument network and data archive for aerosol characterization. Remote Sens. Environ. 66 (1), 1–16.

Holben, B., Tanre, D., Smirnov, A., Eck, T., Slutsker, I., Abuhassan, N., Newcomb, W., Schafer, J., Chatenet, B., Lavenu, F., Kaufman, Y., Castle, J., Setzer, A., Markham, B., Clark, D., Frouin, R., Halthore, R., Karneli, A., O'Neill, N., Pietras, C., Pinker, R., Voss, K., Zibordi, G., 2001. An emerging ground-based aerosol climatology: aerosol optical depth from AERONET. J. Geophys. Res.-Atmos. 106 (D11), 12067–12097.

Huneeus, N., Basart, S., Fiedler, S., Morcrette, J.-J., Benedetti, A., Mulcahy, J., Terradellas, E., Garcia-Pando, C.P., Pejanovic, G., Nickovic, S., 2016. Forecasting the northern African dust outbreak towards Europe in April 2011: a model intercomparison. Atmos. Chem. Phys. 16 (8), 4967.

IPCC, 2001. In: McCarthy, J.J., Canziani, O.F., Leary, N.A., Dokken, D.J., White, K.S. (Eds.), Climate Change 2001: Impacts, Adaptation and Vulnerability, Contribution of Working Group II to the Third Assessment Report of the Intergovernmental Panel on Climate Change. Cambridge University Press, Cambridge, United Kingdom and New York, NY, USA, pp. 1032 (0-521-01500-6).

IPCC, 2013. Summary for Policymakers. In: Stocker, T.F., Qin, D., Plattner, G.-K., Tignor, M., Allen, S.K., Boschung, J. ... Midgley, P.M. (Eds.), Climate Change 2013: The Physical Science Basis. Contribution of Working Group I to the Fifth Assessment Report of the Intergovernmental Panel on Climate Change. Cambridge University Press, Cambridge, United Kingdom and New York, NY, USA.

Khan, B., Stenchikov, G., Weinzierl, B., Kalenderski, S., Osipov, S., 2015. Dust plume formation in the free troposphere and aerosol size distribution during the Saharan Mineral Dust Experiment in North Africa. Tellus B 67 (1). https://doi.org/10.3402/tellusb.v67.27170.

Klein, H., Nickovic, S., Haunold, W., Bundke, U., Nillius, B., Ebert, M., Weinbruch, S., Schuetz, L., Levin, Z., Barrie, L.A., 2010. Saharan dust and ice nuclei over Central Europe. Atmos. Chem. Phys. 10 (21), 10211–10221.

Klett, J.D., 1981. Stable analytical Inversion solution for Processing Lidar returns. Appl. Opt. 20 (2), 211–220.

Lafontaine, C., Bryson, R., Wendland, W., 1990. Airstream regions of North-Africa and the Mediterranean. J. Clim. 3 (3), 366–372.

Mahowald, N., Baker, A., Bergametti, G., Brooks, N., Duce, R., Jickells, T., Kubilay, N., Prospero, J., Tegen, I., 2005. Atmospheric global dust cycle and iron inputs to the ocean. Glob. Biogeochem. Cycles 19 (4).

Mamouri, R.E., Ansmann, A., 2014. Fine and coarse dust separation with polarization

lidar. Atmos. Meas. Tech. 7, 3717–3735. https://doi.org/10.5194/amt-7-3717-2014.
Mamouri, R., Ansmann, A., Nisantzi, A., Kokkalis, P., Schwarz, A., Hadjimitsis, D., 2013. Low Arabian dust extinction-to-backscatter ratio. Geophys. Res. Lett. 40 (17), 4762–4766.
Mamouri, R., Ansmann, A., Nisantzi, A., Solomos, S., Kallos, G., Hadjimitsis, D., 2016. Extreme dust storm over the eastern Mediterranean in September 2015: satellite, lidar, and surface observations in the Cyprus region. Atmos. Chem. Phys. 16 (21), 13711–13724.
Mona, L., Amodeo, A., Pandolfi, M., Pappalardo, G., 2006. Saharan dust intrusions in the Mediterranean area: three years of Raman lidar measurements. J. Geophys. Res.-Atmos. 111 (D16).
Mona, L., Papagiannopoulos, N., Basart, S., Baldasano, J., Binietoglou, I., Cornacchia, C., Pappalardo, G., 2014. EARLINET dust observations vs. BSC-DREAM8b modeled profiles: 12-year-long systematic comparison at Potenza, Italy. Atmos. Chem. Phys. 14 (16), 8781–8793.
Müller, D., Heinold, B., Tesche, M., Tegen, I., Althausen, D., Arboledas, L., Amiridis, V., Amodeo, A., Ansmann, A., Balis, D., 2009. EARLINET observations of the 14-22-May long-range dust transport event during SAMUM 2006: validation of results from dust transport modelling. Tellus B 61 (1), 325–339.
Müller, D., Ansmann, A., Freudenthaler, V., Kandler, K., Toledano, C., Hiebsch, A., Gasteiger, J., Esselborn, M., Tesche, M., Heese, B., Althausen, D., Weinzierl, B., Petzold, A., von Hoyningen-Huene, W., 2010. Mineral dust observed with AERONET Sun photometer, Raman lidar, and in situ instruments during SAMUM 2006: Shape-dependent particle properties. J. Geophys. Res.-Atmos. 115.
Nisantzi, A., Mamouri, R., Ansmann, A., Schuster, G., Hadjimitsis, D., 2015. Middle East versus Saharan dust extinction-to-backscatter ratios. Atmos. Chem. Phys. 15 (12), 7071–7084.
Obregón, M., Pereira, S., Salgueiro, V., Costa, M.J., Silva, A.M., Serrano, A., Bortoli, D., 2015. Aerosol radiative effects during two desert dust events in August 2012 over the Southwestern Iberian Peninsula. Atmos. Res. 153, 404–415.
Pappalardo, G., Amodeo, A., Pandolfi, M., Wandinger, U., Ansmann, A., Bosenberg, J., Matthias, V., Amirdis, V., De Tomasi, F., Frioud, M., Iarlori, M., Komguem, L., Papayannis, A., Rocadenbosch, F., Wang, X., 2004. Aerosol lidar intercomparison in the framework of the EARLINET project. 3. Raman lidar algorithm for aerosol extinction, backscatter, and lidar ratio. Appl. Opt. 43 (28), 5370–5385.
Pappalardo, G., Amodeo, A., Apituley, A., Comeron, A., Freudenthaler, V., Linne, H., Ansmann, A., Bosenberg, J., D'Amico, G., Mattis, I., Mona, L., Wandinger, U., Amiridis, V., Alados-Arboledas, L., Nicolae, D., Wiegner, M., 2014. EARLINET: towards an advanced sustainable European aerosol lidar network. Atmos. Meas. Techniq. 7 (8), 2389–2409.
Pérez, C., Nickovic, S., Pejanovic, G., Baldasano, J., Ozsoy, E., 2006. Interactive dust-radiation modeling: a step to improve weather forecasts. J. Geophys. Res.-Atmos. 111 (D16).
Pérez, C., Haustein, K., Janjic, Z., Jorba, O., Huneeus, N., Baldasano, J., Black, T., Basart, S., Nickovic, S., Miller, R., Perlwitz, J., Schulz, M., Thomson, M., 2011. Atmospheric dust modeling from meso to global scales with the online NMMB/BSC-Dust model - Part 1: model description, annual simulations and evaluation. Atmos. Chem. Phys. 11 (24), 13001–13027.
Pey, J., Querol, X., Alastuey, A., Forastiere, F., Stafoggia, M., 2013. African dust outbreaks over the Mediterranean Basin during 2001–2011: PM 10 concentrations, phenomenology and trends, and its relation with synoptic and mesoscale meteorology. Atmos. Chem. Phys. 13 (3), 1395–1410.
Preissler, J., Wagner, F., Pereira, S., Guerrero-Rascado, J., 2011. Multi-instrumental observation of an exceptionally strong Saharan dust outbreak over Portugal. J. Geophys. Res.-Atmos. 116.
Prospero, J., Ginoux, P., Torres, O., Nicholson, S., Gill, T., 2002. Environmental characterization of global sources of atmospheric soil dust identified with the Nimbus 7 Total Ozone Mapping Spectrometer (TOMS) absorbing aerosol product. Rev. Geophys. 40 (1).
Querol, X., Pey, J., Pandolfi, M., Alastuey, A., Cusack, M., Pérez, N., Moreno, T., Viana, M., Mihalopoulos, N., Kallos, G., 2009. African dust contributions to mean ambient PM10 mass-levels across the Mediterranean Basin. Atmos. Environ. 43 (28), 4266–4277.
Rodríguez-Navarro, C., di Lorenzo, F., Elert, K., 2018. Mineralogy and physicochemical features of Saharan dust wet deposited in the Iberian Peninsula during an extreme red rain event. Atmos. Chem. Phys. 18, 10089–10122. https://doi.org/10.5194/acp-18-10089-2018.
Rolph, G., Stein, A., Stunder, B., 2017. Real-time Environmental applications and Display sYstem: READY. Environ. Model Softw. 95, 210–228.
Salvador, P., Artíñano, B., Molero, F., Viana, M., Pey, J., Alastuey, A., Querol, X., 2013. African dust contribution to ambient aerosol levels across Central Spain: Characterization of long-range transport episodes of desert dust. Atmos. Res. 127, 117–129.
Salvador, P., Alonso-Perez, S., Pey, J., Artinano, B., de Bustos, J., Alastuey, A., Querol, X., 2014. African dust outbreaks over the western Mediterranean Basin: 11-year characterization of atmospheric circulation patterns and dust source areas. Atmos. Chem. Phys. 14 (13), 6759–6775.
Salvador, P., Almeida, S.M., Cardoso, J., Almeida-Silva, M., Nunes, T., Cerqueira, M., Alves, C., Reis, M.A., Chaves, P.C., Artinano, B., Pio, C., 2016. Composition and origin of PM_{10} in Cape Verde: Characterization of long-range transport episodes. Atmos. Environ. 127, 326–339.
Santos, D., Costa, M.J., Silva, A.M., Salgado, R., 2013. Modeling Saharan desert dust radiative effects on clouds. Atmos. Res. 127, 178–194.
Sicard, M., D'Amico, G., Comeron, A., Mona, L., Alados-Arboledas, L., Amodeo, A., Baars, H., Baldasano, J., Belegante, L., Binietoglou, I., Bravo-Aranda, J., Fernandez, A., Freville, P., Garcia-Vizcaino, D., Giunta, A., Granados-Munoz, M., Guerrero-Rascado, J., Hadjimitsis, D., Haefele, A., Hervo, M., Iarlori, M., Kokkalis, P., Lange, D., Mamouri, R., Mattis, I., Molero, F., Montoux, N., Munoz, A., Porcar, C., Navas-Guzman, F., Nicolae, D., Nisantzi, A., Papagiannopoulos, N., Papayannis, A., Pereira, S., Preissler, J., Pujadas, M., Rizi, V., Rocadenbosch, F., Sellegri, K., Simeonov, V., Tsaknakis, G., Wagner, F., Pappalardo, G., 2015. EARLINET: potential operationality of a research network. Atmos. Meas. Tech. 8 (11), 4587–4613.
Sicard, M., Barragan, R., Dulac, F., Alados-Arboledas, L., Mallet, M., 2016. Aerosol optical, microphysical and radiative properties at regional background insular sites in the western Mediterranean. Atmos. Chem. Phys. 16 (18), 12177–12203.
Sorribas, M., Adame, J., Andrews, E., Yela, M., 2017. An anomalous African dust event and its impact on aerosol radiative forcing on the Southwest Atlantic coast of Europe in February 2016. Sci. Total Environ. 583, 269–279.
Stein, A.F., Draxler, R.R., Rolph, G.D., Stunder, B.J.B., Cohen, M.D., Ngan, F., 2015. NOAA's HYSPLIT atmospheric transport and dispersion modeling system. Bull. Am. Meteorol. Soc. 96, 2059–2077.
Titos, G., Ealo, M., Pandolfi, M., Pérez, N., Sola, Y., Sicard, M., Comerón, A., Querol, X., Alastuey, A., 2017. Spatiotemporal evolution of a severe winter dust event in the western Mediterranean: Aerosol optical and physical properties. J. Geophys. Res. Atmos. 122. https://doi.org/10.1002/2016JD026252.
Tsekeri, A., Lopatin, A., Amiridis, V., Marinou, E., Igloffstein, J., Siomos, N., Solomos, S., Kokkalis, P., Engelmann, R., Baars, H., 2017. GARRLiC and LIRIC: strengths and limitations for the characterization of dust and marine particles along with their mixtures. Atmos. Meas. Tech. 10 (12), 4995.
Wagner, F., Bortoli, D., Pereira, S., Costa, M.J., SILVA, A., Weinzierl, B., Esselborn, M., Petzold, A., Rasp, K., Heinold, B., 2009. Properties of dust aerosol particles transported to Portugal from the Sahara desert. Tellus B 61 (1), 297–306.
WMO (World Meteorological Organization), 2011. Weather Extreme in a Changing Climate: Hindsight on Foresight. WMO-No. 1075. (ISBN: 978-92-63-11075-6).